

NACA TN 2749 Title

# NATIONAL ADVISORY COMMITTEE FOR AERONAUTICS

0065879



TECH LIBRARY KAFB, NM

TECHNICAL NOTE 2749

## ANALYSIS OF FLOW IN A SUBSONIC MIXED-FLOW IMPELLER

By Chung-Hua Wu, Curtis A. Brown, and  
Eleanor L. Costilow

Lewis Flight Propulsion Laboratory  
Cleveland, Ohio



Washington

August 1952

AFMDC  
TECHNICAL LIBRARY  
AFL 2811



0065879

1B

## NATIONAL ADVISORY COMMITTEE FOR AERONAUTICS

TECHNICAL NOTE 2749

## ANALYSIS OF FLOW IN A SUBSONIC MIXED-FLOW IMPELLER

By Chung-Hua Wu, Curtis A. Brown, and  
Eleanor L. Costilow

2405

## SUMMARY

A method recently developed for determining the steady flow of a nonviscous compressible fluid along a relative stream surface extending from hub to casing between two adjacent blades in a turbomachine is applied to investigate the through flow of air in an experimental mixed-flow impeller of high solidity. The shape of the stream surface is taken to be the same as that of the mean camber surface of the blade which consists of all radial elements. The principal equation governing the through flow is solved by the relaxation method with the use of fourth-degree differentiation formulas for unequally spaced grid points caused by the varying hub and casing wall radii.

A detailed analysis is made of both incompressible and compressible flow through the impeller, and contour plots of the stream function, velocity components, total enthalpy, static pressure, and Mach number are presented and discussed. The trends of flow variations in the impeller for the incompressible and compressible solutions are quite similar. The trend in the variation of static pressure along the casing obtained in the compressible solution compares very well with the experimental data obtained under the same operating condition.

## INTRODUCTION

The axial-discharge mixed-flow compressor possesses the theoretical potentiality of an optimum combination of high pressure ratio, high specific mass flow, flat operating characteristics, light weight, compactness, and durability. In conjunction with the experimental investigation of this type of compressor undertaken at the NACA Lewis laboratory, a method capable of analyzing accurately the nonviscous compressible through flow (reference 1) was developed and applied to the theoretical flow in the experimental impeller shown in figure 1. A brief account of a compressible solution obtained by this method is given in reference 2.

A brief description of the method of analysis is presented herein considering the mean stream surface approach advanced in references 2 and 3, and both the incompressible and compressible solutions are given in detail. The usefulness of the incompressible solution (which is obtainable much more quickly than the compressible solution) is evaluated and the available experimental data of pressure variation along the casing are compared with the theoretical solution obtained without and with an approximate correction for the effect of blade thickness. (For a more accurate correction for the effect of blade thickness on the through flow and for a complete three-dimensional flow analysis, the method given in reference 3 can be used.)

2405

### SYMBOLS

The following symbols are used in this report:

- a velocity of sound
- B blade thickness factor
- $\frac{m_B^i}{n_j}$  differentiation coefficients in equation (12) used to multiply function value at point  $x_j$  to give  $m^{\text{th}}$  derivative at  $x_i$  based on  $n^{\text{th}}$  degree polynomial
- $g_1(z)$   $\frac{d\phi}{dz}$
- H total enthalpy per unit mass,  $h + \frac{1}{2} V^2$
- h static enthalpy per unit mass
- I  $h + \frac{1}{2} w^2 - \frac{1}{2} \omega^2 r^2 = H - \omega(V_u r)$
- J,K,N function of  $r$  and  $z$  (equation (11))
- M Mach number
- n unit vector normal to mean stream surface
- P blade pitch or spacing
- p static pressure
- r,φ,z cylindrical coordinates relative to impeller

2405

S mean stream surface  
s entropy per unit mass of air  
T temperature  
t time  
U velocity of blade, or  
V absolute velocity of air  
W velocity of air relative to impeller  
r ratio of specific heats of air, 1.4  
ρ density of gas  
τ blade thickness in circumferential direction  
ψ stream function defined on stream surface  
ω angular velocity of impeller

## Subscripts:

c casing  
e exit  
h hub  
i inlet  
 $r, u, z$  radial, circumferential, and axial components, respectively  
T total, or stagnation, state  
t tip

## Superscript:

\* dimensionless quantity

2405

## METHOD OF ANALYSIS

## Equations Governing Flow on Mean Stream Surface

A general idea of the average air flow through the mixed-flow impeller is best obtained by determining the flow from hub to casing along the mean stream surface, which circumferentially divides the mass flow in the channel formed by two adjacent blades into two equal portions (fig. 1). Because the impeller has very high solidity blades, for an approximate solution this mean stream surface may be assumed to have the same shape as that of the mean camber surface of the blade. With the shape of the surface known, the angular coordinate of the surface  $\varphi$  is then, in general, a given function of the two other cylindrical coordinates  $r$  and  $z$ . However, as usual in mixed-flow and radial-flow impellers, the mean camber surface of the blade consists of all radial elements, a fact which renders  $\varphi$  a function of  $z$  only.

If

$$\varphi = f(z) \quad (1)$$

and

$$\frac{d\varphi}{dz} = g_1(z) \quad (2)$$

(using the same notation as in reference 3), then

$$\frac{W_u}{W_z} = - \frac{n_z}{n_u} = r g_1(z) \quad (3)$$

and

$$W_u n_u + W_z n_z = 0 \quad (4)$$

These four equations give the special properties for this type of flow surface. The turning function  $g_1$  together with the hub and casing shape completely defines the impeller.

Because the elements of the flow surface are all radial, the use of cylindrical coordinates results in considerable simplification in the determination of the flow along the surface. With the "blade force" in the radial direction equal to zero, the two other components need not be evaluated during the calculation, and the solution of the problem is obtained by solving the following differential equation in a stream function  $\psi$ , which is defined on the stream surface (see reference 3):

$$\left[1 + (rg_1)^2\right] \frac{\partial^2 \psi}{\partial r^2} - \frac{1 - (rg_1)^2}{r} \frac{\partial \psi}{\partial r} + \frac{\partial^2 \psi}{\partial z^2} - \left\{ \left[1 + (rg_1)^2\right] \frac{\partial \ln B_0}{\partial r} \frac{\partial \psi}{\partial r} + \frac{\partial \ln B_0}{\partial z} \frac{\partial \psi}{\partial z} \right\} + 2g_1 \omega r^2 B_0 + \frac{(rB_0)^2}{\partial \psi / \partial r} \left( -\frac{\partial I}{\partial r} + T \frac{\partial s}{\partial r} \right) = 0 \quad (5)$$

2405

in conjunction with the relation between density and  $\psi$ -derivatives

$$\frac{\rho}{\rho_{T,i}} = \left\{ \frac{I + \frac{\omega^2 r^2}{2}}{H_i} - \frac{\left[1 + (rg_1)^2\right] \left(\frac{\partial \psi}{\partial r}\right)^2 + \left(\frac{\partial \psi}{\partial z}\right)^2}{2(rB_0)^2 H_i} \right\}^{\frac{1}{\gamma-1}} e^{s_{T,i}-s} \quad (6)$$

In the preceding equations,  $r$  and  $z$  are the two independent variables and the bold derivative sign refers to the differentiation following the stream surface. The stream function  $\psi$  on the stream surface is related to the meridional velocity components of the air flowing along the stream surface by the following equations:

$$W_r = -\frac{1}{rB_0} \frac{\partial \psi}{\partial z} \quad (7)$$

$$W_z = \frac{1}{rB_0} \frac{\partial \psi}{\partial r} \quad (8)$$

In equations (5) to (8),  $B$  is actually related to the angular variation of the air velocities and the shape of the stream surface by

$$\ln \frac{B}{B_1} = \int_{t_1}^t \frac{1}{n_u r} \left( n_u \frac{\partial W_u}{\partial \phi} + n_z \frac{\partial W_z}{\partial \phi} \right) dt \quad (9)$$

in which the integration is performed along a streamline. In reference 3,  $B$  is also shown to be proportional to the angular thickness of a stream filament whose mean surface is the stream surface considered herein. In general,  $B$  can be determined by the method given in reference 3. At the start of the present investigation, however, this method was unavailable and  $B$  was taken to be 1. The solution based on  $B = 1$  becomes exact when the ratio of circumferential thickness of the blade to the pitch approaches zero. In using this solution as an approximate solution for thick blades, the effect of

SCFZ  
5

blade thickness should be properly corrected. (Results obtained in reference 4 indicate that this factor  $B$  is closely related to the channel width ratio  $(P-\tau)/P$ . Inasmuch as the channel width ratio decreases toward 1 along the radius in the impeller, it is expected that the streamlines for the actual blade would everywhere rise above those obtained with  $B = 1$ .)

In the solution of equation (5), the variations of  $I$  and  $s$  are determined by the values at the inlet to the blade and the fact that  $I$  and  $s$  remain constant along the streamline for adiabatic steady relative flow of a nonviscous fluid. The values are considered to be radially uniform at the inlet to the blade in the present solution, and consequently are uniform everywhere. The computation of density according to equation (6) is greatly simplified by the use of the general density table given in reference 3. For the simplified case of incompressible flow, equation (5) is solved using a constant value of density.

Equation (5) is the principal equation to be solved for the region of flow where the function  $g_1$  is known from the blade shape. Upstream and downstream of the impeller,  $g_1$  is not known and therefore equation (5) is replaced by the following equation (references 1 to 3):

$$\frac{\partial^2 \psi}{\partial r^2} - \frac{1}{r} \frac{\partial \psi}{\partial r} + \frac{\partial^2 \psi}{\partial z^2} - \left( \frac{\partial \ln B_p}{\partial r} \frac{\partial \psi}{\partial r} + \frac{\partial \ln B_p}{\partial z} \frac{\partial \psi}{\partial z} \right) + \frac{(rB_p)^2}{\frac{\partial \psi}{\partial r}} \left[ \frac{w_u}{r} \frac{\partial (v_{ur})}{\partial r} - \frac{\partial I}{\partial r} + T \frac{\partial s}{\partial r} \right] = 0 \quad (10)$$

in which the radial variations of  $v_{ur}$  are determined from its value far upstream of the impeller (equal to zero in the present case) and at the exit of the impeller, respectively, and from the condition that it remains constant along a streamline in the absence of blade action or of a circumferential pressure gradient. In the present solution, the radial derivative of  $v_{ur}$  is zero upstream of the impeller and is not equal to zero downstream of the impeller.

#### Method of Solution

Equation (5) or (10) is first written in a common form

$$J \frac{\partial^2 \psi}{\partial r^2} + K \frac{\partial \psi}{\partial r} + \frac{\partial^2 \psi}{\partial z^2} = N \quad (11)$$

The derivatives in equation (11) are then approximated by an appropriate finite-difference expression. In the present analysis, a grid size on the meridional plane as shown in figure 2 is chosen, and fourth-degree polynomial representation is used. The finite-difference form of equation (11) at grid point  $i$  (fig. 2) is

$$\sum_{j=0}^4 \left( J \frac{2}{4} \frac{B_i}{j} + K \frac{1}{4} \frac{B_i}{j} \right) \psi_j + \sum_{k=0}^4 \frac{2}{4} \frac{B_i}{j} \psi_k = N \quad (12)$$

where  $\psi_j$  and  $\psi_k$  denote the values of  $\psi$  on the surface corresponding to the grid points along constant- $z$  and  $-r$  lines, respectively, on the meridional plane. In order to fit the grid points on the hub and casing walls at both ends of the impeller, it is necessary to use two grid sizes in the  $r$  direction (0.3544 in the inlet portion and 0.2650 in the exit portion). At the time this investigation was begun, the tables of differentiation coefficients for unequal grid size given in reference 5 were unavailable, and the differentiation coefficients were computed from the formula given in that reference.

In the present analysis, the system of finite-difference equation (12) covering the entire domain is solved by the relaxation method of Southwell (reference 6) with the modification described in reference 5. Because  $N$  in the equation is dependent on the unknown  $\psi$ , the solution must be improved through successive corrections. Sufficiently accurate results are obtained herein by making only three cycles of calculation. For a quicker and more accurate answer and especially for investigations where many similar cases are to be analyzed, it is desirable to employ the matrix method or another method on high-speed digital machines (references 5 and 7). Detailed steps of the matrix method of solution are given in reference 7.

In the present calculations, all quantities are rendered dimensionless as follows:

$$r^* = \frac{r}{r_{t,i}} ; z^* = \frac{z}{r_{t,i}} ; \rho^* = \frac{\rho}{\rho_{t,i}} ; W^* = \frac{W}{U_{t,i}} ; H^* = \frac{H}{U_{t,i}^2}$$

## RESULTS AND DISCUSSION

### Incompressible Solution

The incompressible solution was first obtained for use as the starting value of the compressible solution and for evaluating the usefulness of the incompressible solution for this type of compressor.

Prescribed conditions. - The variation of  $g_1$  or  $d\phi/dz$  directly computed from the mean camber surface of the experimental blade is shown in figure 3. It is smoothed out slightly and corrected at the exit for a slip factor of 0.95, which is used in the original design.

The value of  $g_1$  at the leading edge of the blade is -0.287. The incompressible solution is therefore good when the inlet Mach number is low and when

$$V_z^* = \frac{V_{z,i}}{U_{t,i}} = \frac{1}{0.287 r_{t,i}} = 0.625$$

or

$$\omega = 0.287 V_{z,i}$$

The results obtained in the incompressible solution are presented in figures 4 to 9. Overlays of the contour plots for the compressible solution discussed later are attached and may be used for comparison with the contour plots for the incompressible solution.

Streamlines. - Figure 4 shows the streamlines for 10 equal divisions of the mass flow. The position of the streamlines is seen to be mainly determined by the shapes of the hub and casing. With respect to their geometrical relation at the inlet, they are first raised by the positive curvature of the hub wall and then lowered by the negative curvature of the casing wall. (In this respect, it would be interesting to compare the streamlines in fig. 4 with the streamlines obtained for  $g_1$  equal to zero everywhere, that is, an axially symmetric flow in the annulus with no tangential velocity.)

Variation of velocity components. - In figure 5(a), contours of constant values of  $V_{z,i}$  are superposed on the streamlines. Because of the relative shift in the streamline mentioned in the preceding paragraph and the general decrease in channel area, the axial velocity of the air above the 0.3 streamline increases in the inducer section, decreases from  $z \approx 1.1$  inches to  $z \approx 3.0$  inches, and then increases toward the exit; whereas the axial velocity of the air below the 0.3 streamline decreases in the inducer section and increases from there on. The air enters with a uniform axial velocity ratio of 0.625 and leaves with a radial profile decreasing from 1.11 at the hub to 0.91 at the casing.

The variations of radial velocity shown in figure 5(b) resulted from a direct combination of the slopes of the streamlines and the variation in axial velocity. The maximum value of radial velocity ratio

is equal to 0.66 along the hub wall at a short distance downstream of the point of maximum slope. It then decreases rapidly along the hub toward the exit.

The variation of relative tangential velocity in the impeller is shown in figure 5(c). At the leading edge of the blade, the velocity varies almost linearly with the radius because the elements of the stream surface are all radial and the axial velocity on the surface is nearly constant. This simple radial pattern is gradually distorted by the variations in axial velocity. At the trailing edge of the blade, the relative tangential velocity is nearly zero.

The variation of the magnitude of resultant relative velocity is shown in figure 5(d). At the leading edge, it increases with the radius because of the increase in its tangential component. Toward the exit where the tangential component is very small, its variation is similar to that of the axial component. Between the two ends, its variation is a combination of the variations of the two components.

Between the 0 and the 0.4 streamlines, the magnitude of the resultant relative velocity decreases in the inducer section and then increases toward the exit. Between the 0.5 and the 1.0 streamlines, it fluctuates along the streamline. The variation of velocity along the casing and the hub is shown separately in figure 6. This local rise of velocity along the casing around  $z = 1.2$  inches apparently is caused by the earlier rise of hub radius than casing radius.

Variation of total enthalpy. - The greater change in tangential velocity at the tip (fig. 5(c)) overcomes the greater rise in radius at the hub and results in a positive radial gradient of total enthalpy with increasing magnitude from the inlet to  $z = 5$  inches (fig. 7). However, the extra turning at the lower radii between  $z = 5$  inches and  $z = 6$  inches causes the total enthalpy to have a negative radial gradient leaving the impeller. This overcompensation in total enthalpy is due to the triangular trailing portion of the blade, which was designed for a different inlet flow. For this operating condition, a radially constant total enthalpy would be obtained downstream of the impeller if the blade terminates at, for example, the 1.4 constant total enthalpy line.

Variation of static pressure. - The fact that  $I$  remains constant along a streamline for adiabatic steady relative flow of a nonviscous fluid gives, for incompressible flow,

$$\frac{p}{\rho} + \frac{w^2}{2} - \frac{\omega^2 r^2}{2}$$

constant along a streamline. At the inlet to the blade, because  $V_{ur}$  is zero, this expression is equal to  $H_1$ . Hence

$$\frac{p}{\rho} = H_1 - \frac{w^2}{2} + \frac{\omega_r^2 r^2}{2}$$

or

$$\frac{\frac{p}{\rho} - H_1}{2} = \frac{r^*2 - w^*2}{2}$$

$$\frac{p}{\rho_t, i} = \frac{r^*2 - w^*2}{2}$$

2405

In this form, the static pressure can be computed for any inlet values (within the range of applicability of incompressible flow) of  $H_1$ ,  $\rho$ , and the blade speed. Constant values of this generalized pressure parameter are shown in figure 8. Below the 0.4 streamline, the static pressure of air rises along its streamline when  $z < 2$  inches and decreases when  $z > 2$  inches. Above the 0.5 streamlines, the static pressure at first rises, drops to a minimum at  $z \approx 1$  inch, and rises again to a maximum near  $z = 4.5$  inches. The variation of pressure along the casing and hub is separately shown in figure 9. For a local rise of velocity along the casing at  $z \approx 1.2$  inches, there is a corresponding local drop of static pressure. This local drop of static pressure is undesirable in that it gives a high rate of increase in the main portion of the impeller for the same over-all rise in pressure across the impeller, and it may be the cause of the relatively low efficiency obtained in the experimental tests of this impeller.

Downstream of the impeller, the pressure parameter has a positive radial gradient (from -0.1654 to 0.31 at casing).

#### Compressible Solution

Prescribed conditions. - In the compressible solution, an inlet Mach number of 0.45 is chosen, which gives a maximum relative Mach number in the impeller of about 0.8 at the tip of the leading edge. The flow throughout the impeller is subsonic. For this inlet Mach number,

$$\left( \frac{p}{\rho_t} \right)_i = 0.9055$$

$$\frac{H_1}{U_{t,i}^2} = 4.997$$

The equivalent impeller tip speed at the exit is 987 feet per second. The first approximate solution of the compressible case gives streamlines having oscillatory motion of large magnitude near the leading edge of the impeller, which may be caused by the sudden imposition of the 0.287 value of  $g_1$  at the leading edge of the impeller. The variation of  $g_1$  is therefore smoothed and extended upstream according to the variation of turning along a mean streamline obtained in reference 4 (see fig. 18 of reference 4). This modification is shown in figure 3.

As evidenced in the incompressible solution, overturning of the air may result at the hub of the trailing edge because the inlet flow used in this solution is different from that of the original design; it therefore seems best to remove the triangular section at the trailing edge and to determine the flow with a radial trailing edge ending at  $z = 5.5$  inches. The resulting radial gradient in total enthalpy there will indicate how the extra turning should be added. The meridional section of the modified impeller used in this solution is shown in figure 10.

Streamlines. - Figure 10 also shows the streamlines obtained in the final compressible solution. In general, they lie above the incompressible ones, as required by the density term in the principal equation (5) or (10).

Variation of velocity components. - The contour plots of the velocity components, the resultant velocity, and the velocity at the walls (figs. 11 and 12) are seen to be of shapes similar to the incompressible ones. Their magnitudes, however, are generally lower than the incompressible ones and the difference increases toward the exit. This lower value of the velocity is a combined result of the radially outward shift of streamline position and the increase in density in the impeller toward the exit.

Variation of total enthalpy. - The contours of total enthalpy (fig. 13) again are similar to those obtained in the incompressible solution. The values are higher than those for the incompressible ones, because a lower value of  $W_u$  gives a larger change of the angular momentum of the air from its inlet value at any point in the impeller.

Variation of static pressure. - For compressible flow, the ratio of static pressure to inlet total pressure is directly obtained by raising the corresponding density ratio to the 1.4 power. The shape of the contours shown in figure 14 is similar to that shown in figure 8 for the incompressible case. There is again a local drop of pressure along the casing near  $z = 1.1$  inches (fig. 15) due to the local rise in velocity. This local drop in pressure can be avoided by increasing the casing radius around that location.

Variation of Mach number. - The contours of relative Mach number in the impeller are shown in figure 16. The curves are seen to be similar to those of the resultant velocity. For the inlet absolute Mach number of 0.45, the maximum relative Mach number was found to be equal to 0.805 at the tip radius at the leading edge of the blade. The exit relative Mach number varies from 0.70 to 0.50 from hub to tip, corresponding to an absolute Mach number varying from 1.0 to 0.95.

2045

#### Usefulness of Incompressible Solution

The similarity between the flow variations obtained for incompressible and compressible flow makes the quickly obtainable incompressible solution valuable in giving a good qualitative picture for the compressible case.

### COMPARISON OF THEORETICAL AND EXPERIMENTAL VARIATION

#### OF STATIC PRESSURE ALONG CASING WALL

During the experimental investigation of the mixed-flow compressor, the static pressure along the casing was obtained for the original impeller running at the speed and inlet condition used in the theoretical compressible solution (without the modification of an impeller at the exit as used in this calculation). The variation of pressure obtained for two mass flows bridging the mass flow of the theoretical solution is shown in figure 17. The theoretical variation obtained with the assumption that  $B$  is equal to 1 everywhere is also shown in the figure. The trends of variation of the two results is seen to be quite similar, and the theoretical value is seen to be higher than the experimental value for the same mass flow. This difference in magnitude is due partly to the approximation that  $B$  is equal to 1 everywhere. Actually, the value of  $B$  should increase from hub to casing in accordance with the practically uniform blade thickness and the directly increasing circumferential spacing. A more accurate solution of the present problem would require at least three blade-to-blade solutions of flow along three stream filaments of revolution from hub to casing (reference 3). For the present, only an approximate correction of the variation in  $B$  is taken at the casing as follows:

It is assumed that the values of  $\partial\Psi/\partial r$  and  $\partial\Psi/\partial z$  determined with  $B$  equal to 1 everywhere are the same as those obtained with an accurate variation of  $B$ , and that  $B$  is equal to  $(P-\tau)/P$ . The result is also shown in figure 17.

This approximate thickness correction reduces the static pressure at the casing less than it should because, as shown in figure 18, actually  $\frac{\partial \psi}{\partial r}$  is less for  $B = 1$  everywhere than for a solution in which a correct variation in  $B$  is included, for with a correct variation in  $B$  the streamline would shift toward the casing. This shift results in a lesser increase in  $W$  and hence a lesser drop in static pressure toward the exact value. Another part of the difference between the theoretical and experimental values is attributed to the neglect of viscous effects in the theoretical solution.

#### CONCLUDING REMARKS

The results obtained in the present analysis indicate that the general method developed for the solution of through flow in turbomachines offers a useful tool for analyzing the mean flow through the mixed-flow impeller, and that the general trend of compressible flow variations can be determined by an incompressible solution, which is much easier to obtain than the compressible solution.

The trend in the variation of static pressure along the casing agrees well with the experimental data. The local drop in static pressure along the casing at the end of the inducer section is attributed to the reduction in the normal distance of the stream filament of revolution at the casing, which is caused by the rise of hub radius in the inducer section. This local static-pressure drop can be avoided by increasing the casing radius near the location in question.

Lewis Flight Propulsion Laboratory  
National Advisory Committee for Aeronautics  
Cleveland, Ohio, January 20, 1952

#### REFERENCES

1. Wu, Chung-Hua: A General Through-Flow Theory of Fluid Flow With Subsonic or Supersonic Velocity in Turbomachines of Arbitrary Hub and Casing Shapes. NACA TN 2302, 1951.
2. Wu, Chung-Hua: A General Theory of Three-Dimensional Flow with Subsonic and Supersonic Velocity in Turbomachines Having Arbitrary Hub and Casing Shapes. Part II. Paper No. 50-A-79, presented at the Ann. Meeting A.S.M.E. (New York), Nov. 27-Dec. 1, 1950.
3. Wu, Chung-Hua: A General Theory of Three-Dimensional Flow in Subsonic and Supersonic Turbomachines of Axial-, Radial-, and Mixed-Flow Types. NACA TN 2604, 1952.

4. Wu, Chung-Hua, and Brown, Curtis A.: A Method of Analysis for Compressible Flow Past Arbitrary Turbomachine Blades On General Surface of Revolution. NACA TN 2407, 1951.
5. Wu, Chung-Hua: Formula and Table of Coefficients for Numerical Differentiation with Function Values Given at Unequally Spaced Points and Application to Solution of Partial Differential Equations. NACA TN 2214, 1950.
6. Southwell, R. V.: Relaxation Method in Theoretical Physics. Clarendon Press (Oxford), 1946.
7. Wu, Chung-Hua: Matrix and Relaxation Solutions that Determine Subsonic Through Flow in an Axial-Flow Gas Turbine. NACA TN 2750, 1952.

2405

2405

NACA TN 2749

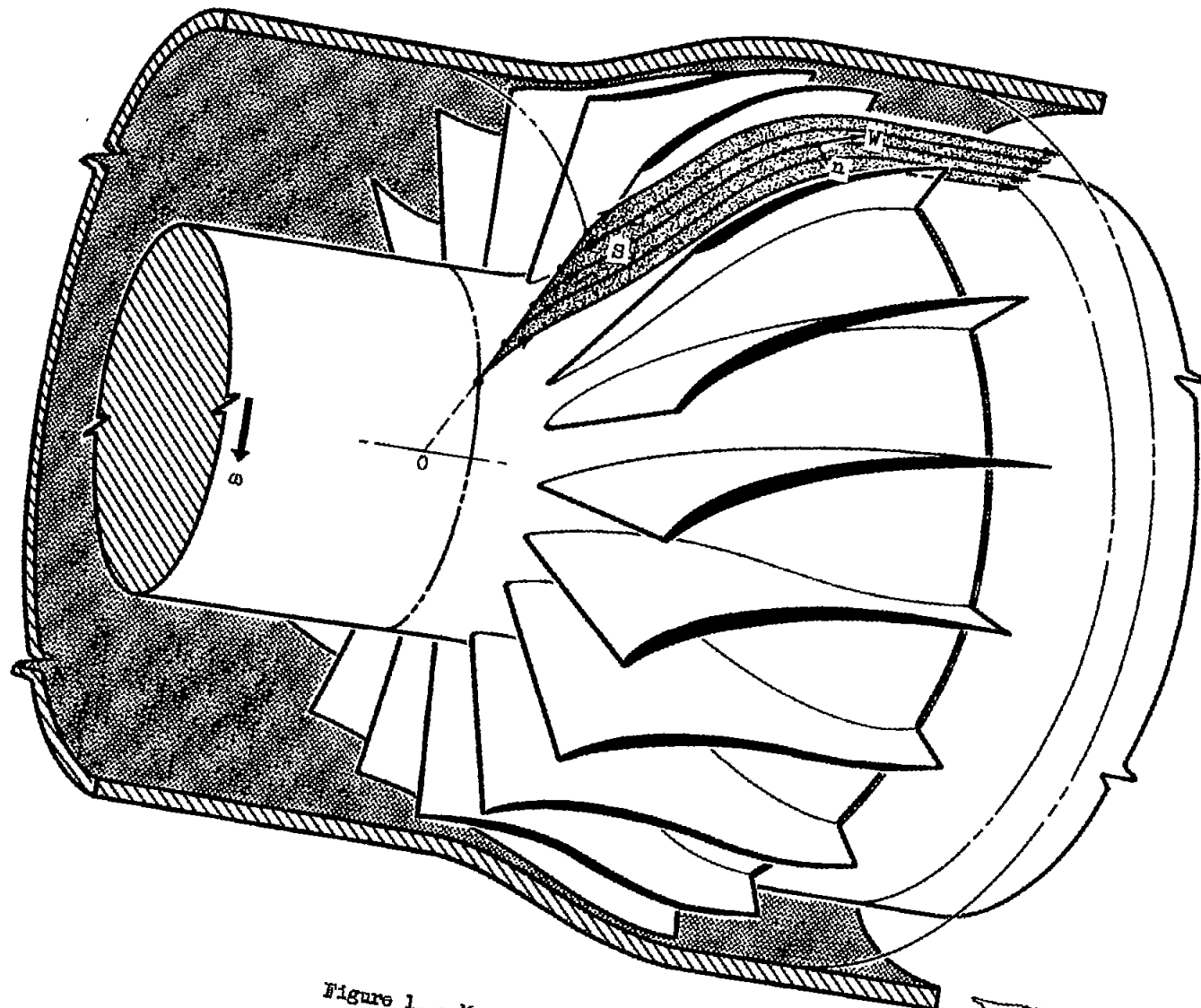


Figure 1. - Mean stream surface  $S$ .

NACA  
CD-2185

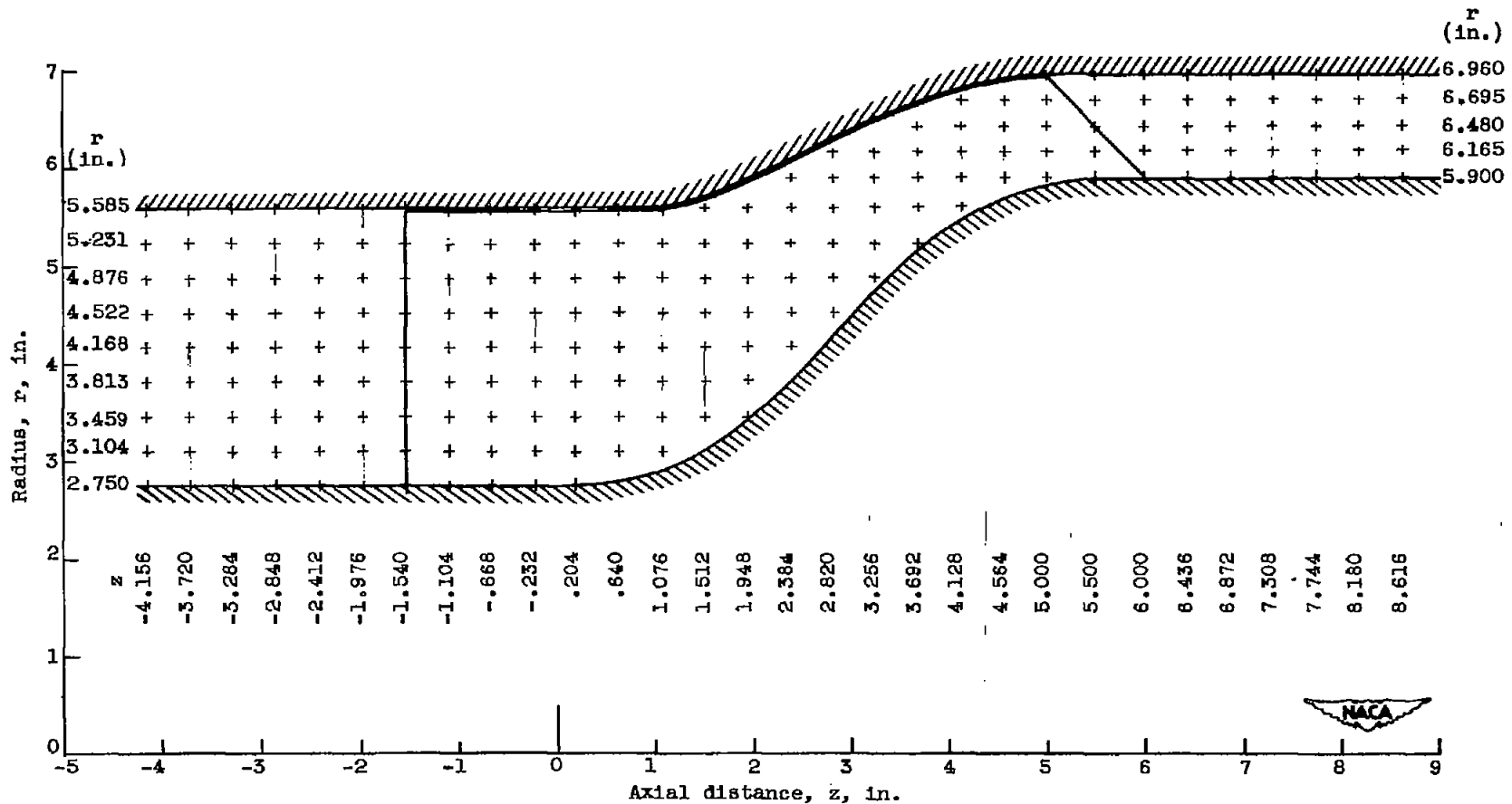
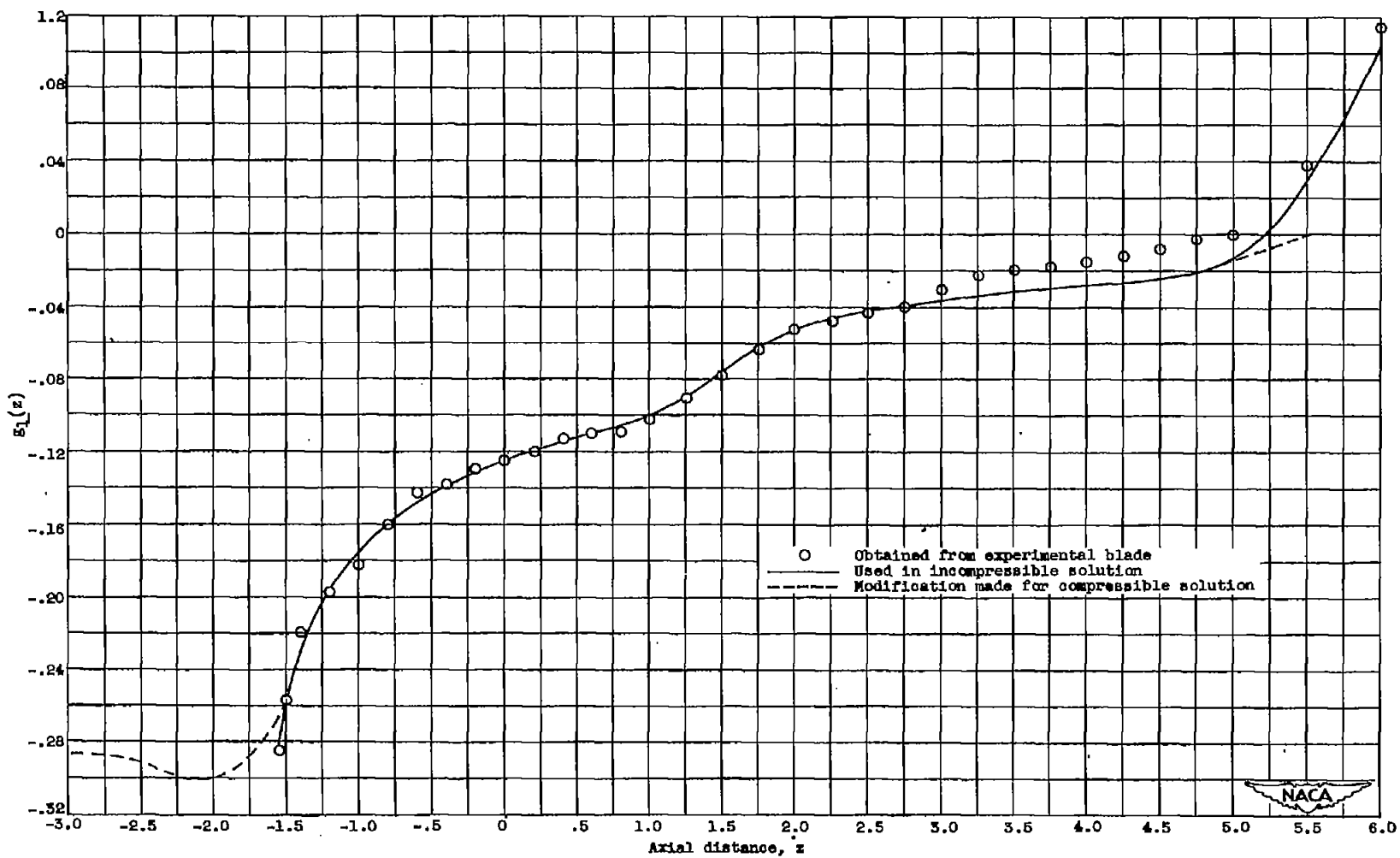


Figure 2. - Meridional section of impeller and grid coordinates on meridional plane.

Figure 3. - Function  $g_1(z)$ .

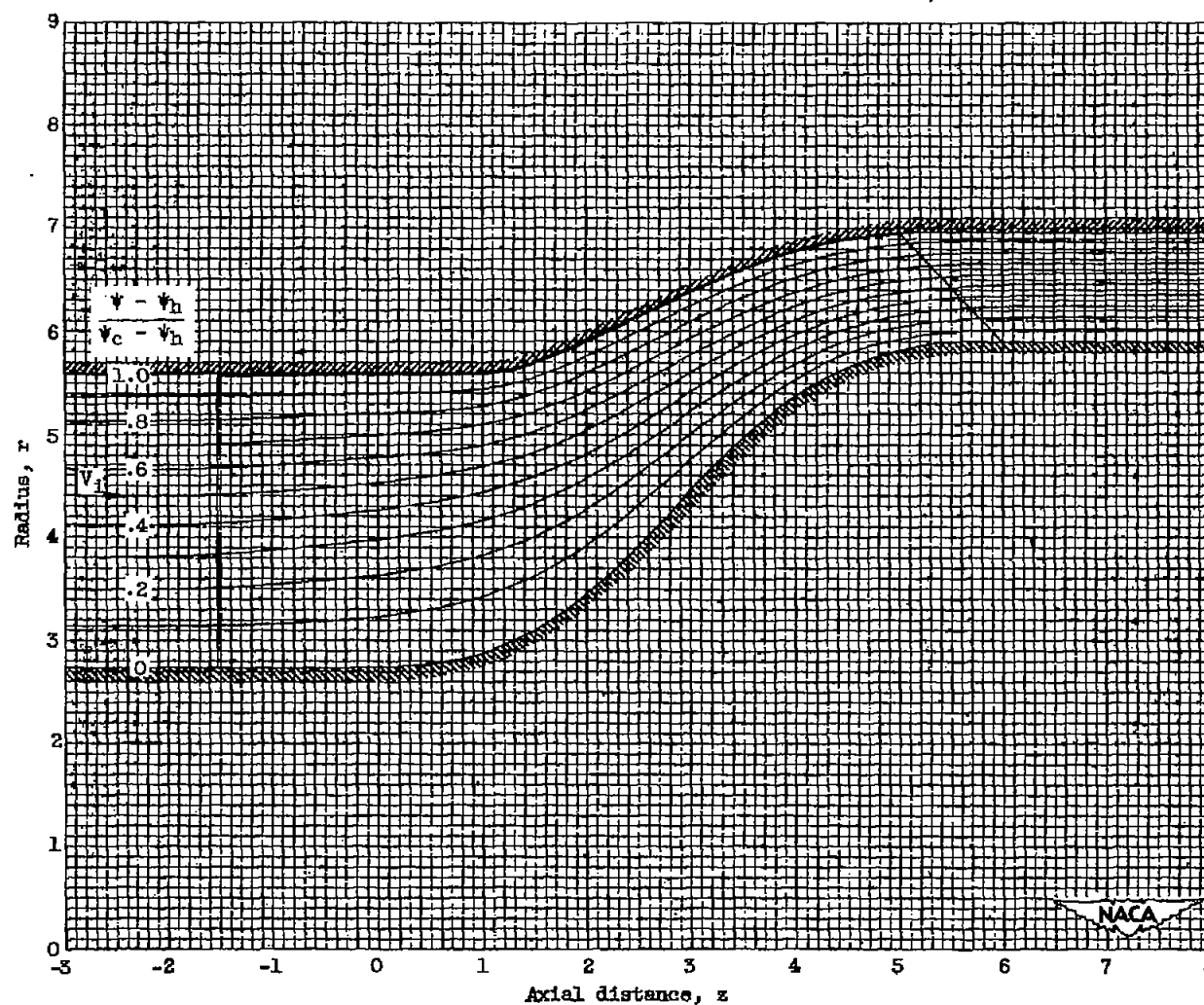
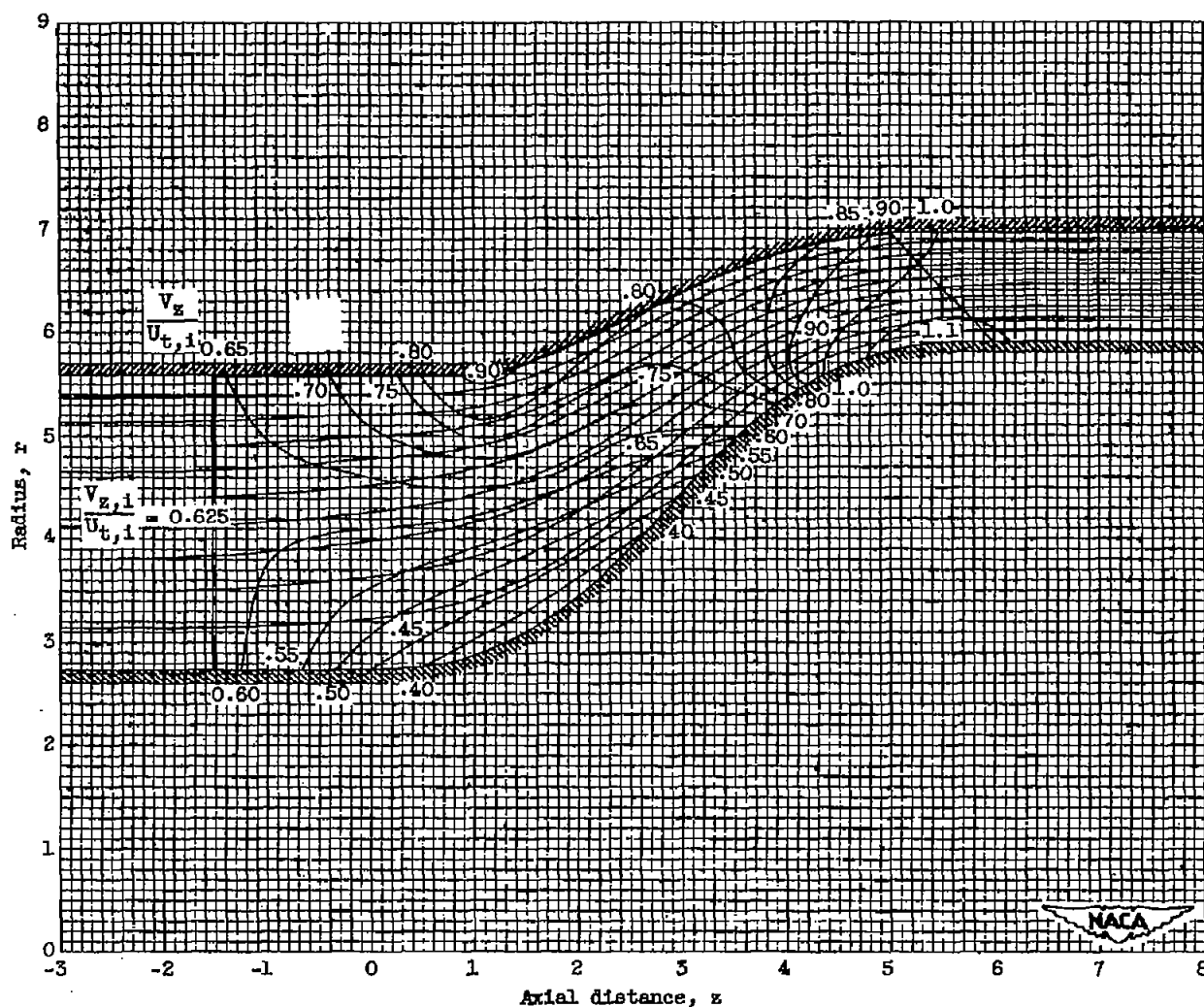
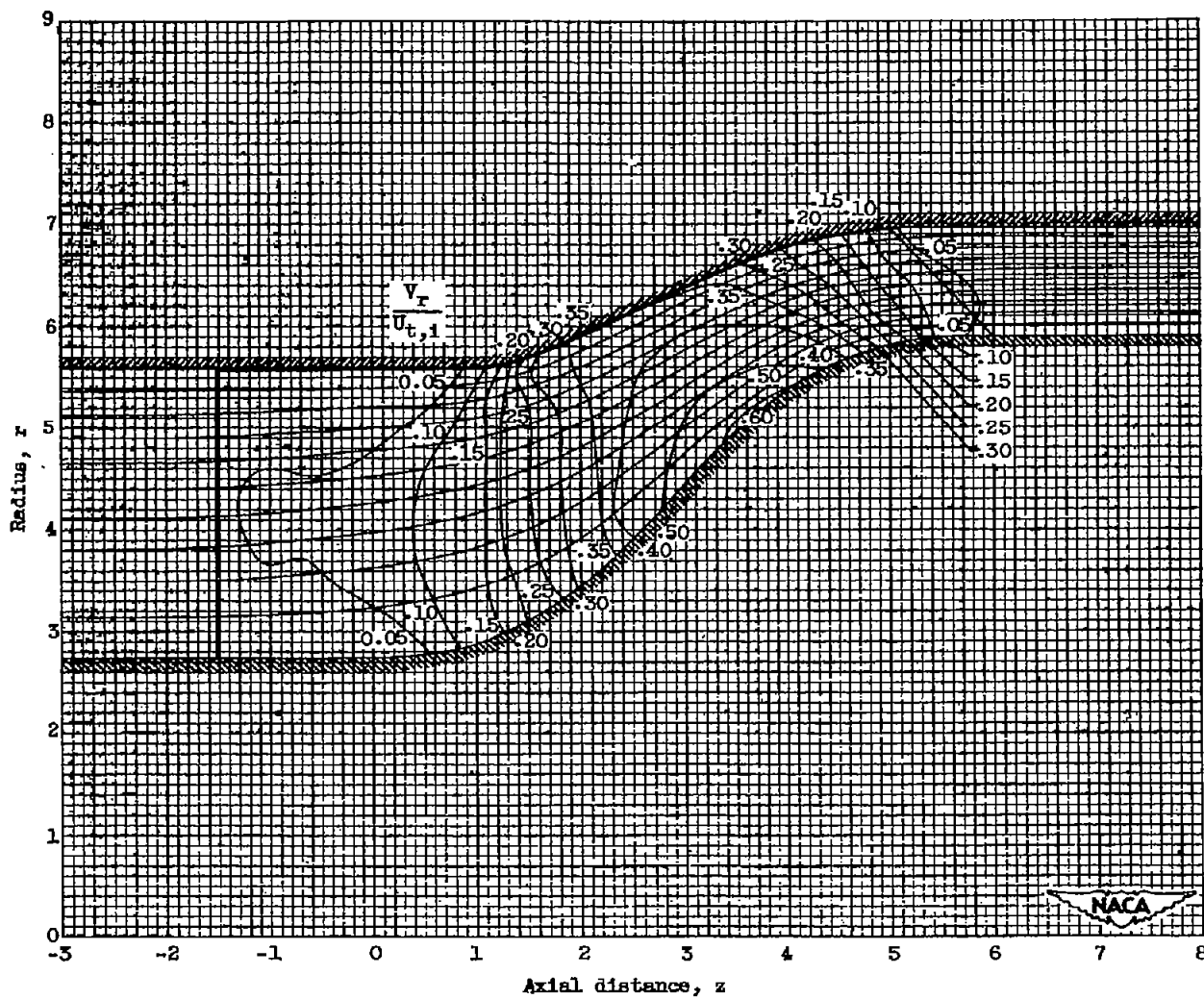


Figure 4. - Meridional projection of streamlines obtained in incompressible solution.



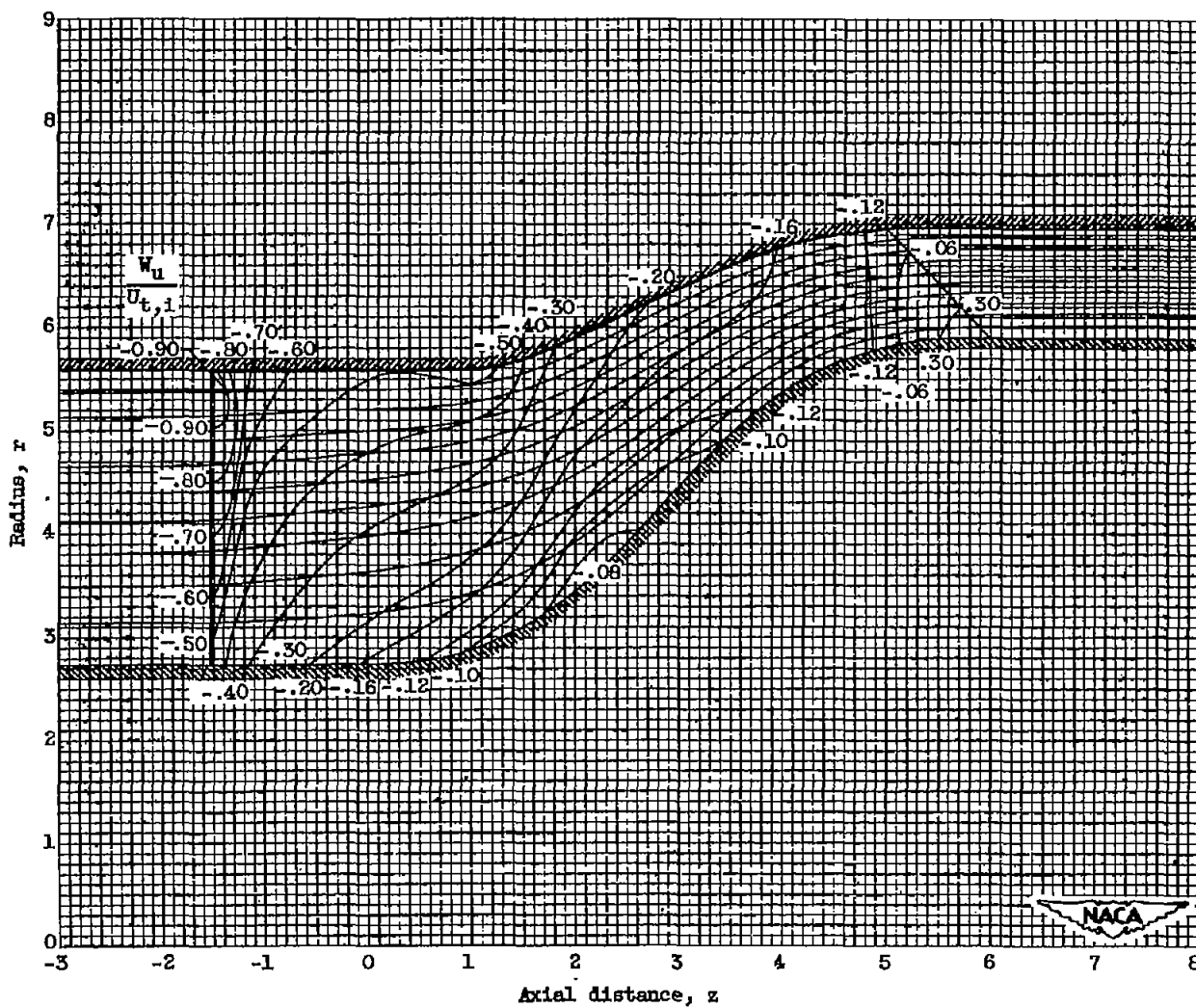
(a) Axial component.

Figure 5. - Meridional projections of constant velocity contours superposed on streamlines for incompressible solution.



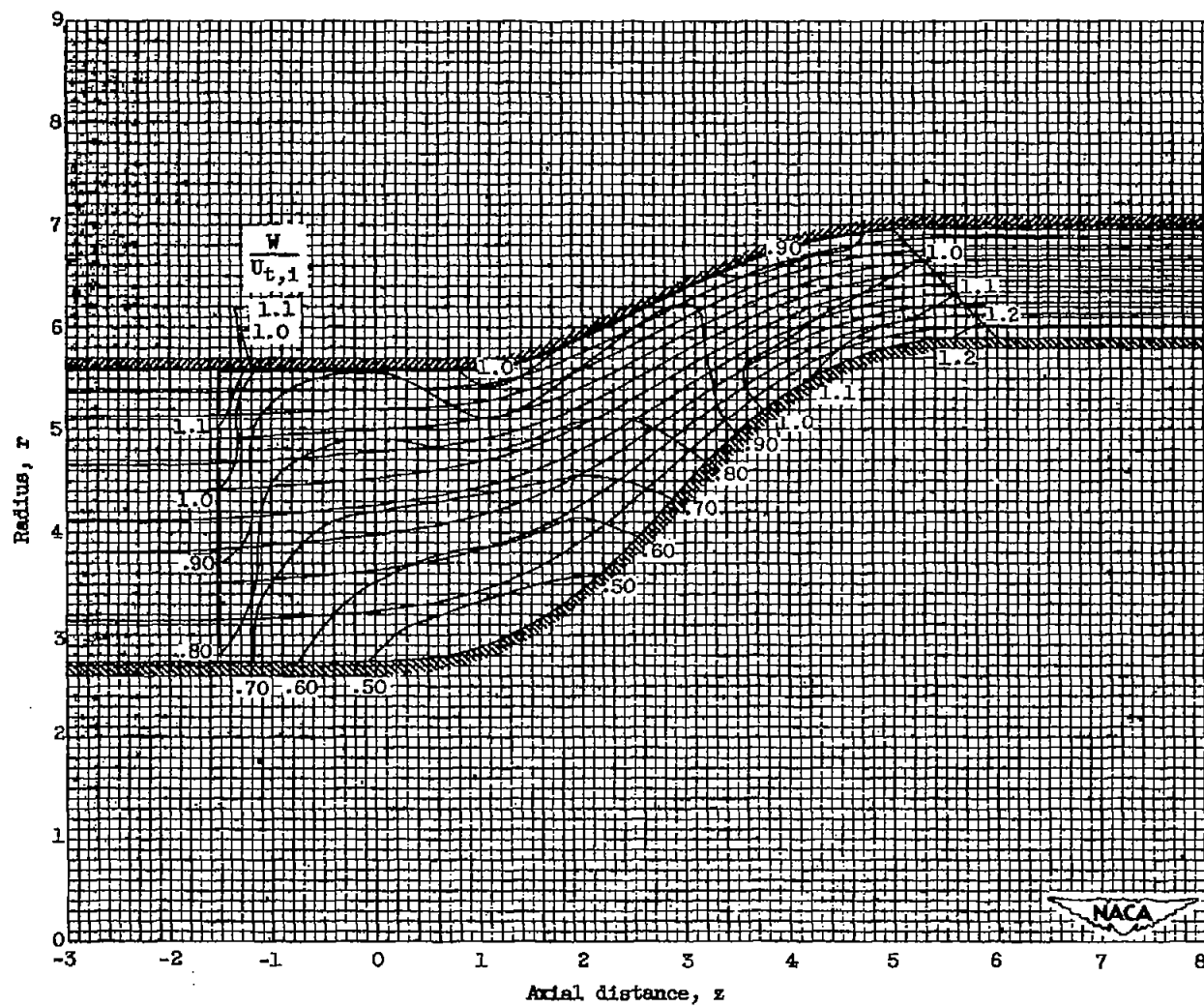
(b) Radial component.

Figure 5. - Continued. Meridional projection of constant velocity contours superposed on streamlines for incompressible solution.



(c) Tangential component.

Figure 5. - Continued. Meridional projection of constant velocity contours superposed on streamlines for incompressible solution.



(d) Resultant relative velocity.

Figure 5. - Concluded. Meridional projection of constant velocity contours superposed on streamlines for incompressible solution.

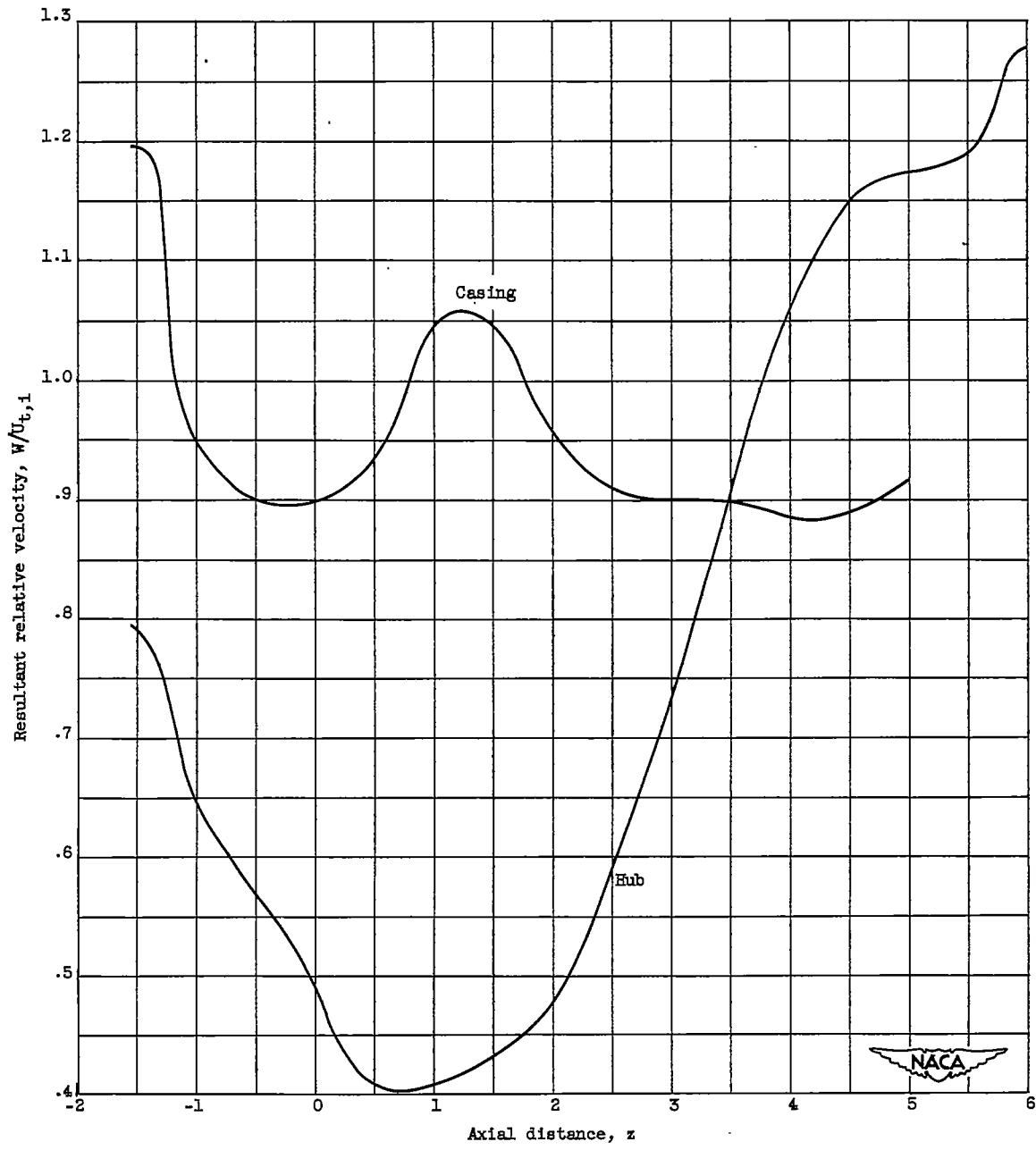


Figure 6. - Variation of magnitude of resultant relative velocity along casing and hub walls for incompressible solution.

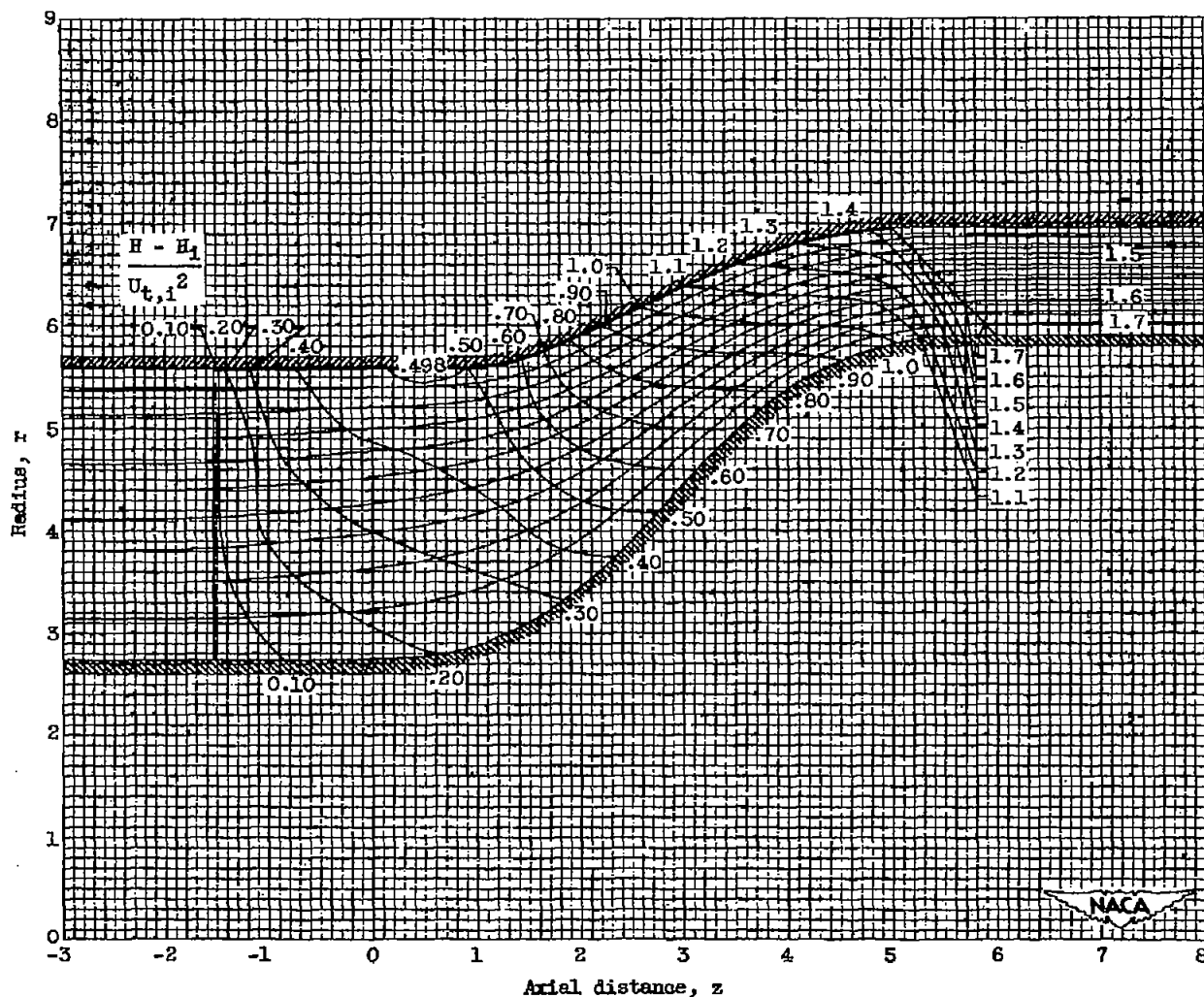


Figure 7. - Meridional projection of contours of constant total enthalpy superposed on streamlines for incompressible solution.

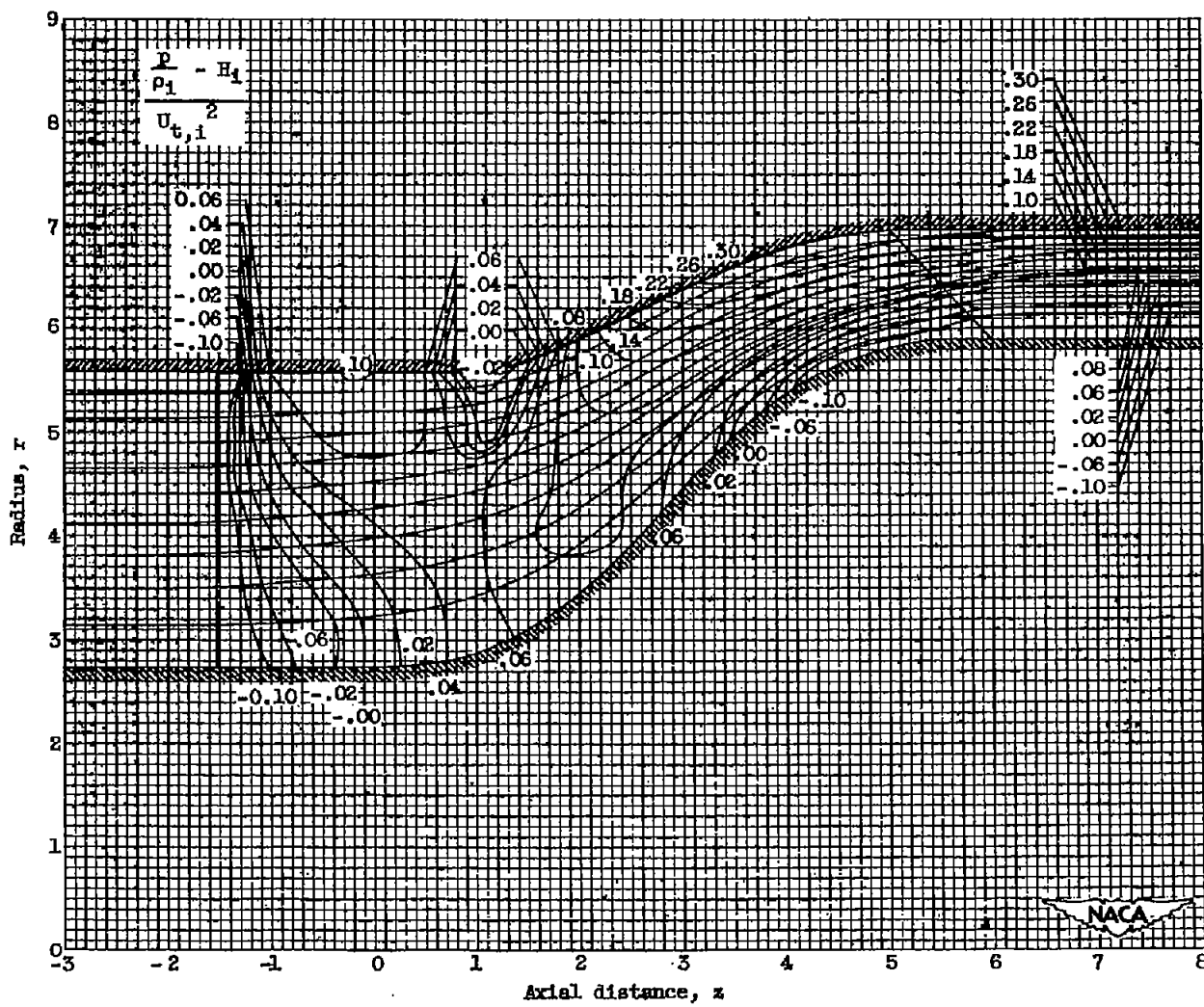


Figure 8. - Meridional projection of contours of constant pressure function superposed on streamlines for incompressible solution.

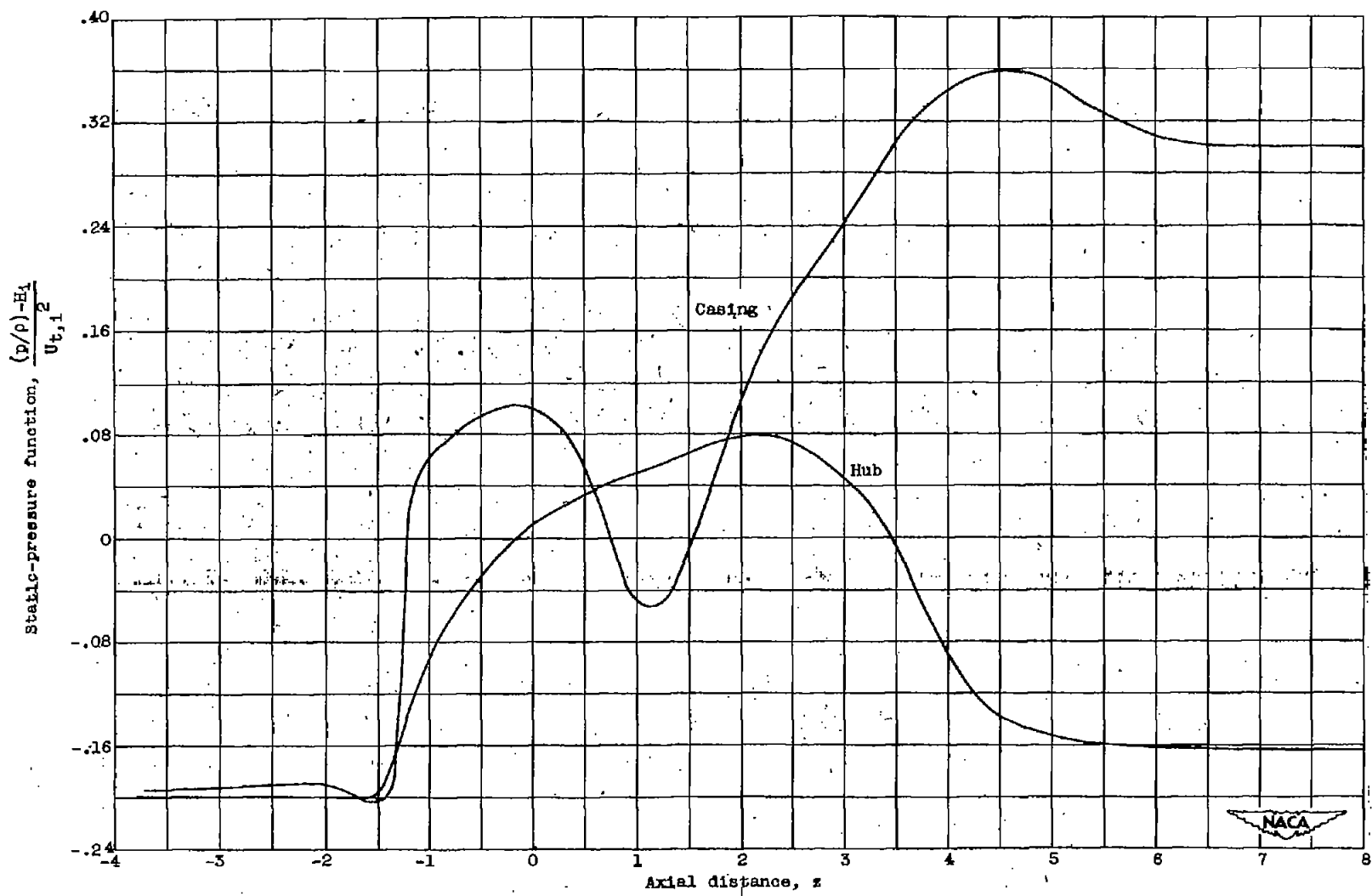


Figure 9. Variation of static-pressure function along casing and hub walls for incompressible solution.

2405

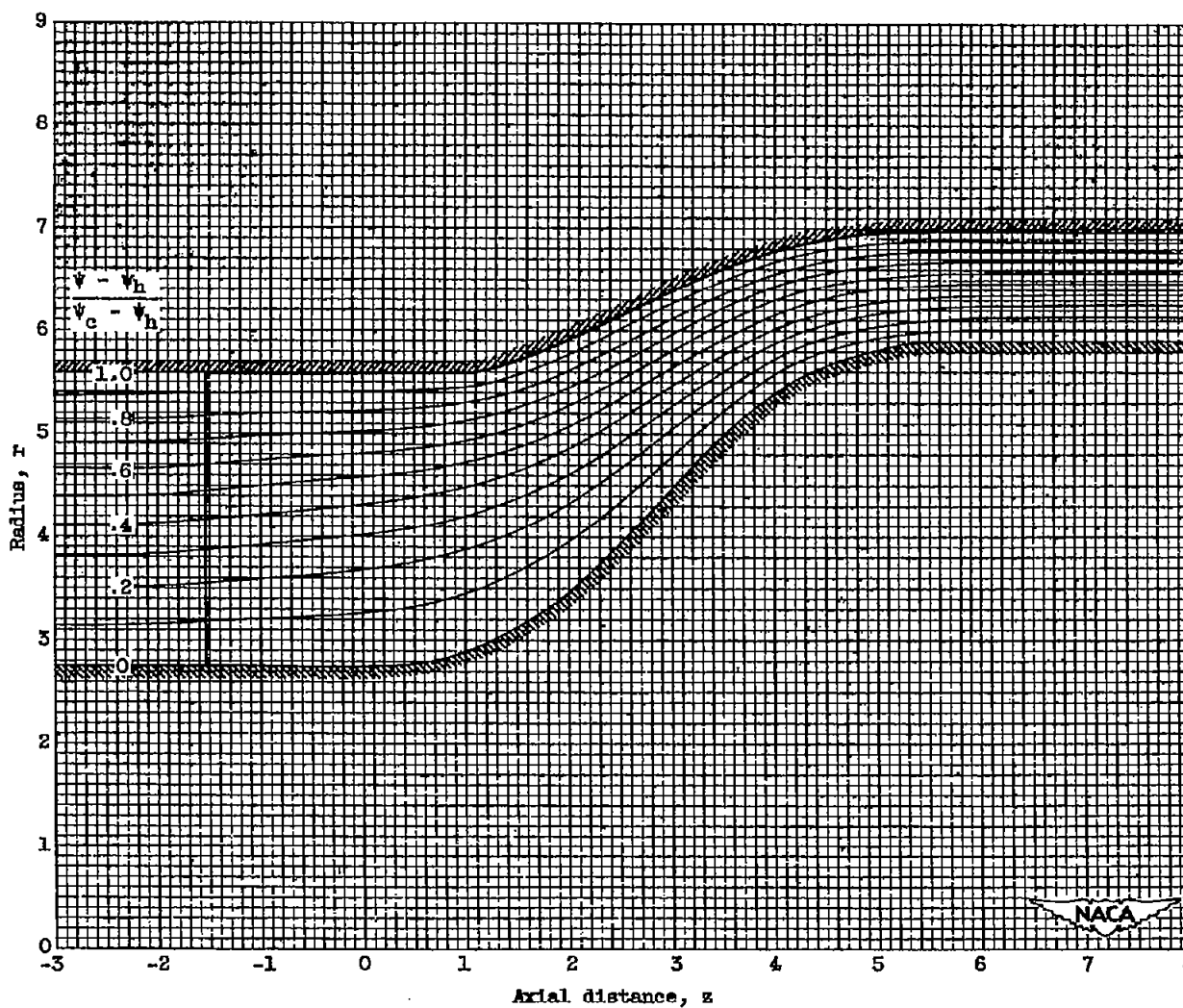
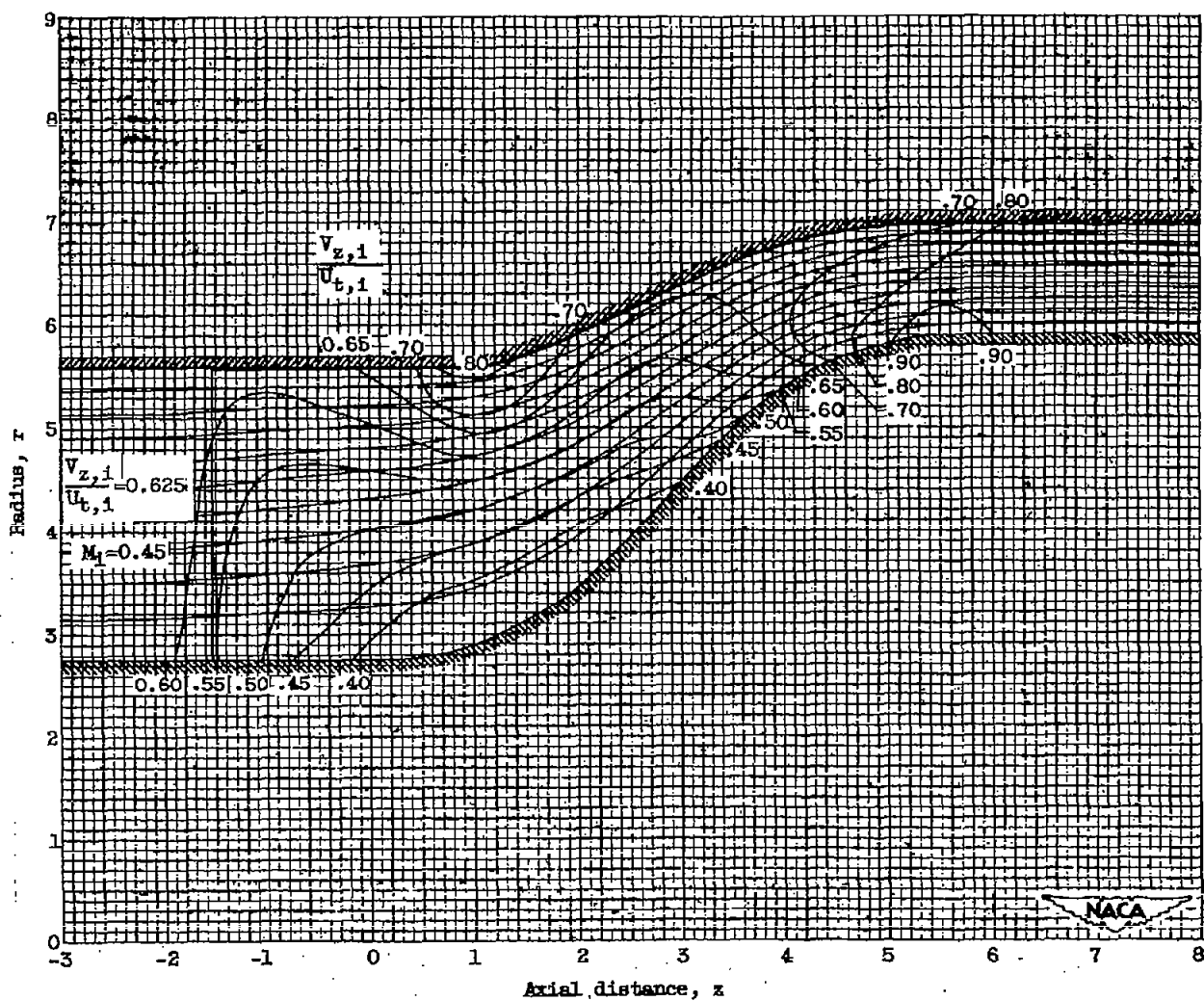


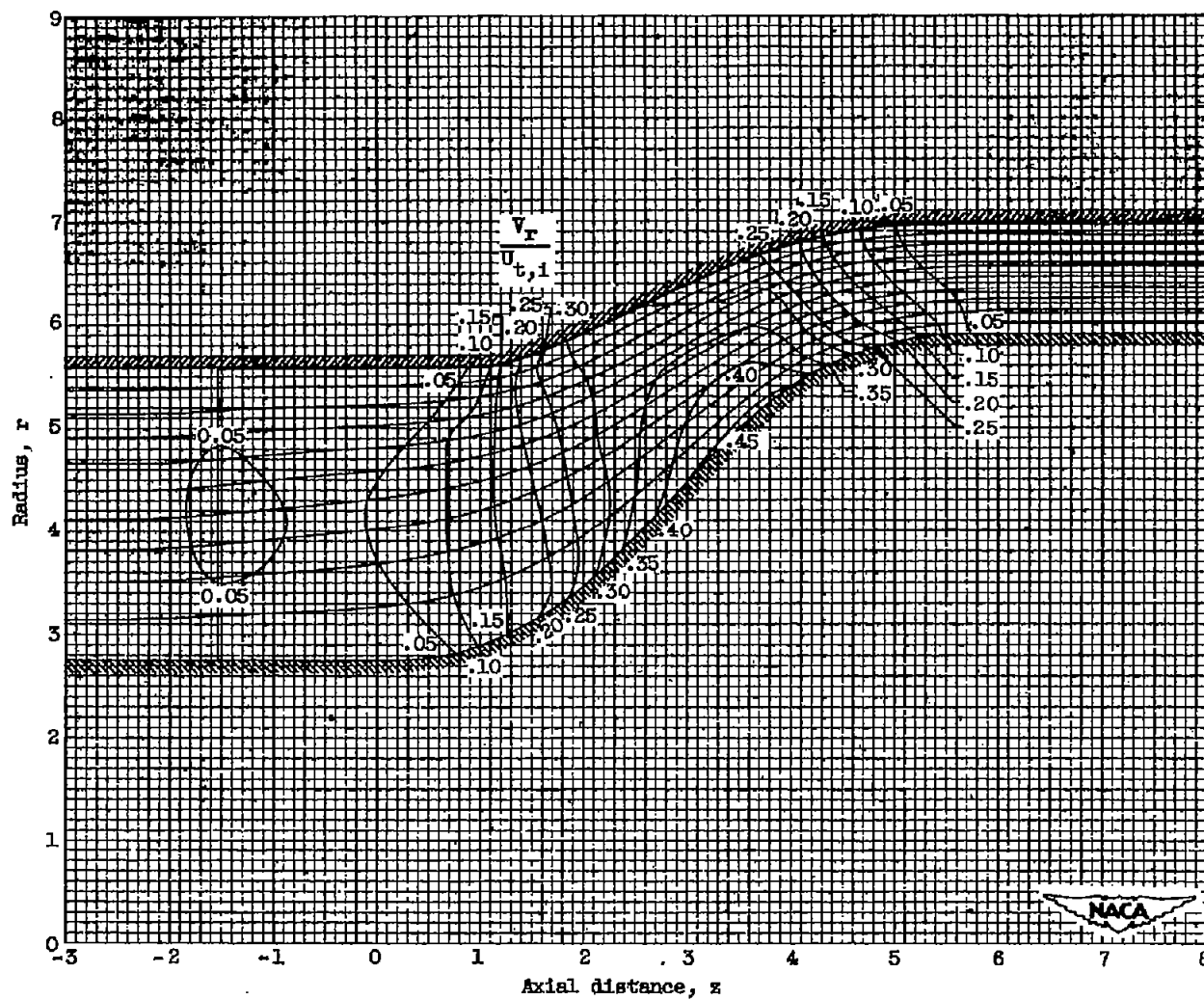
Figure 10.- Meridional projection of streamlines obtained in compressible solution. (An overlay of this fig. is enclosed.)



(a) Axial component.

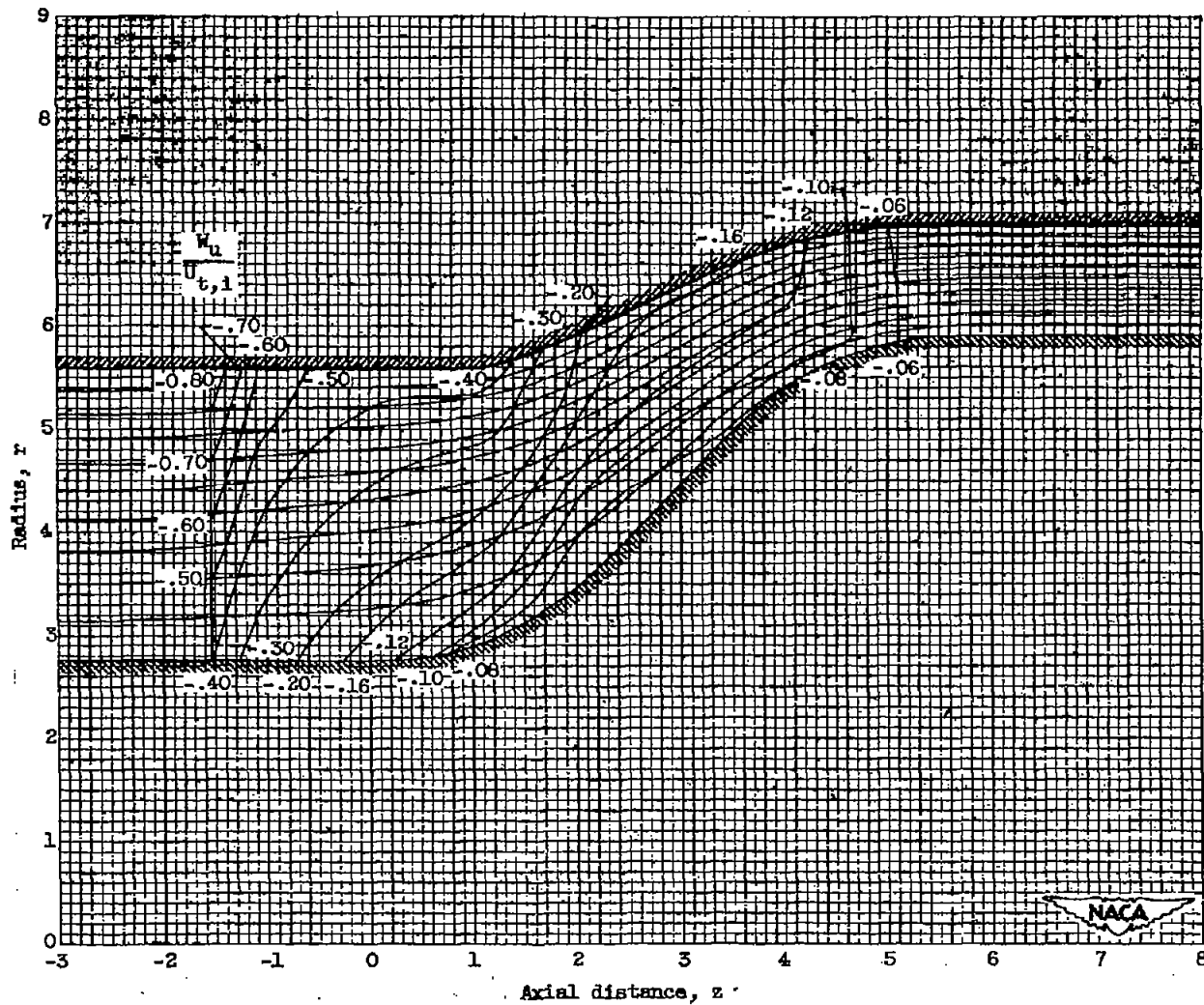
Figure 11.- Meridional projections of constant velocity contours superposed on streamlines for compressible solution. (An overlay of this fig. is enclosed.)

2405



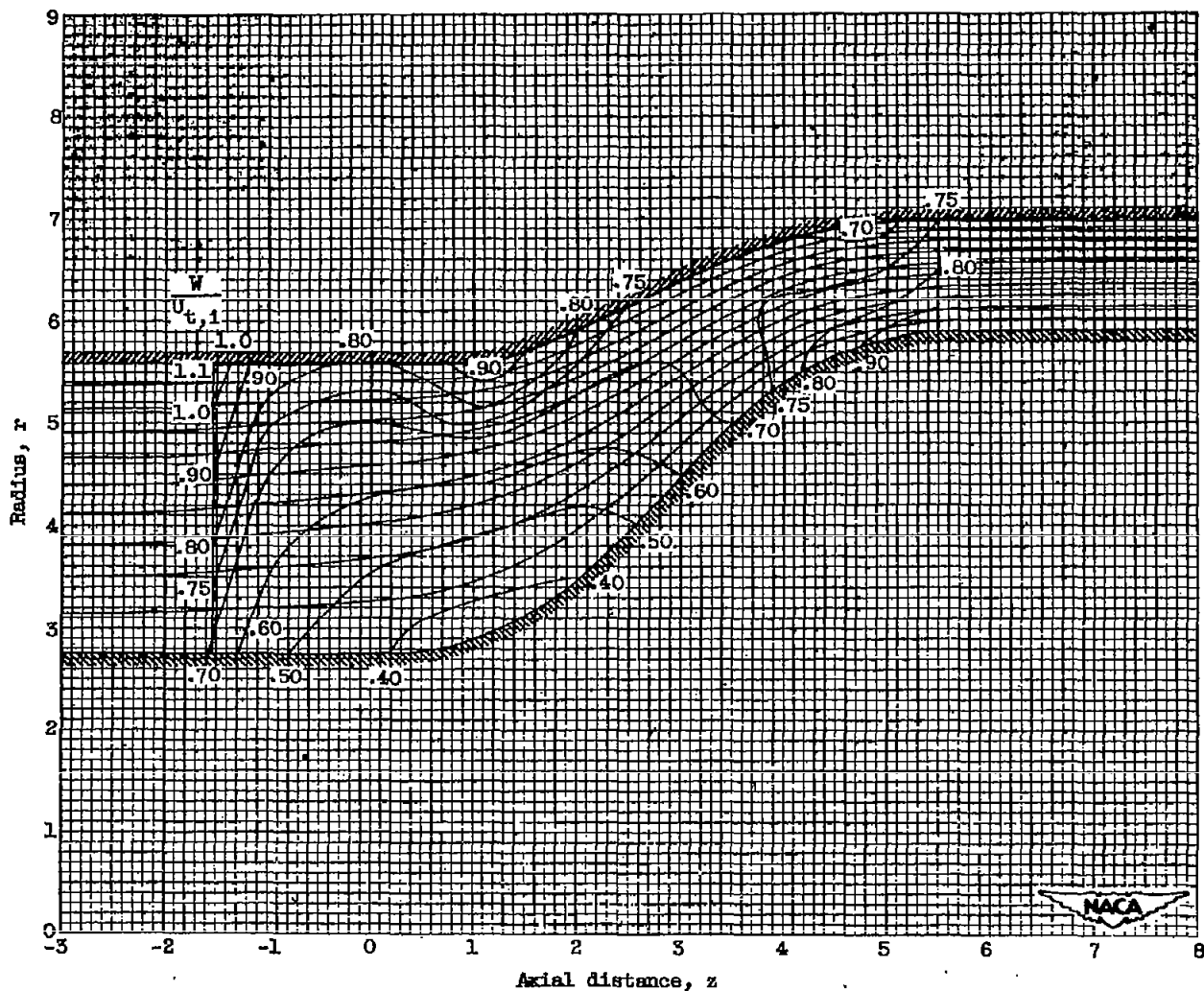
(b) Radial component.

Figure 11.- Continued. Meridional projections of constant velocity contours superposed on streamlines for compressible solution. (An overlay of this fig. is enclosed.)



(c) Tangential component.

Figure 11.- Continued. Meridional projections of constant velocity contours superposed on streamlines for compressible solution. (An overlay of this fig. is enclosed.)



(d) Resultant relative velocity.

Figure 11.- Concluded. Meridional projections of constant velocity contours superposed streamlines for compressible solutions. (An overlay of this fig. is enclosed)

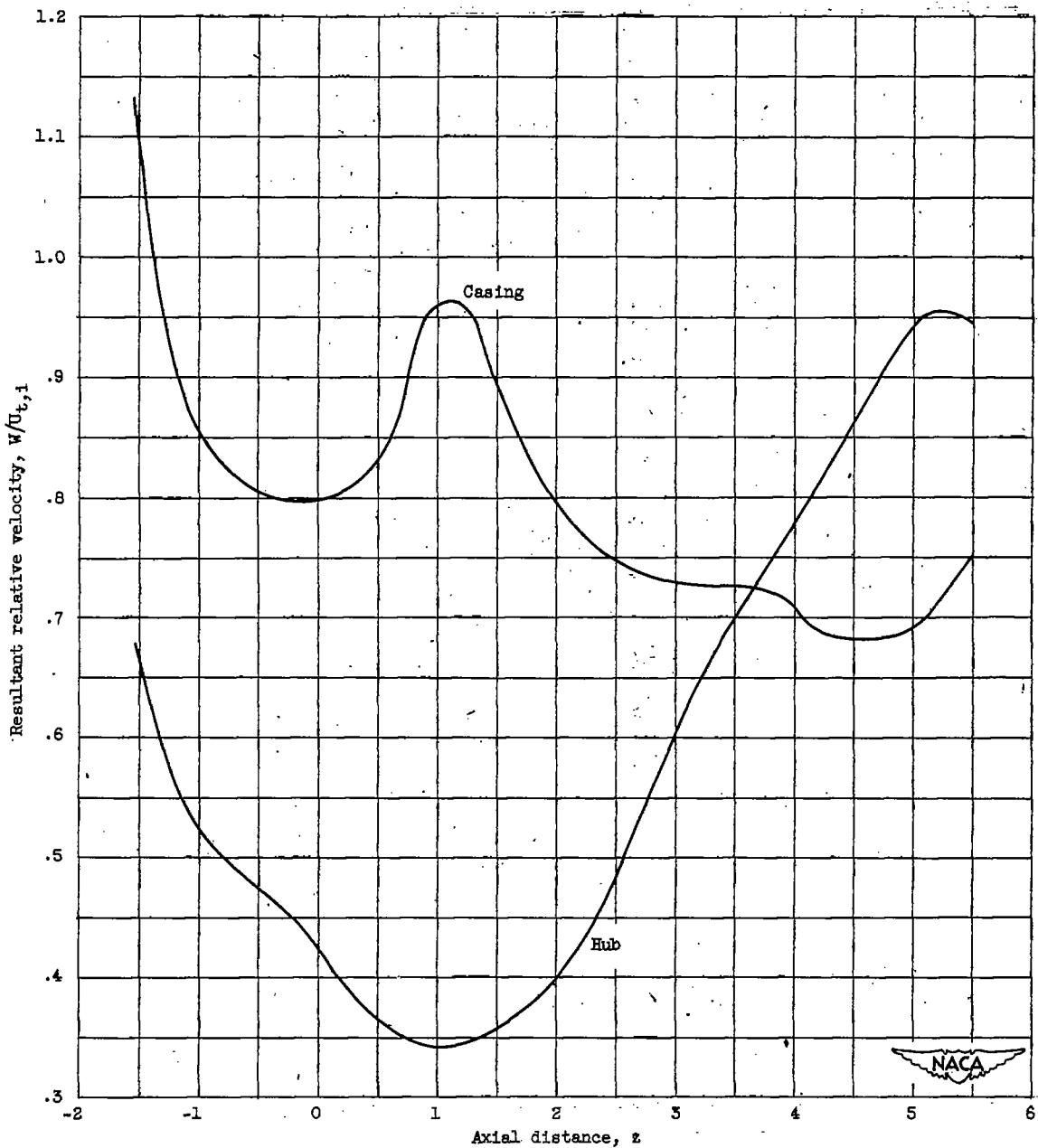


Figure 12. - Variation of magnitude of resultant relative velocity along casing and hub walls for compressible solution.

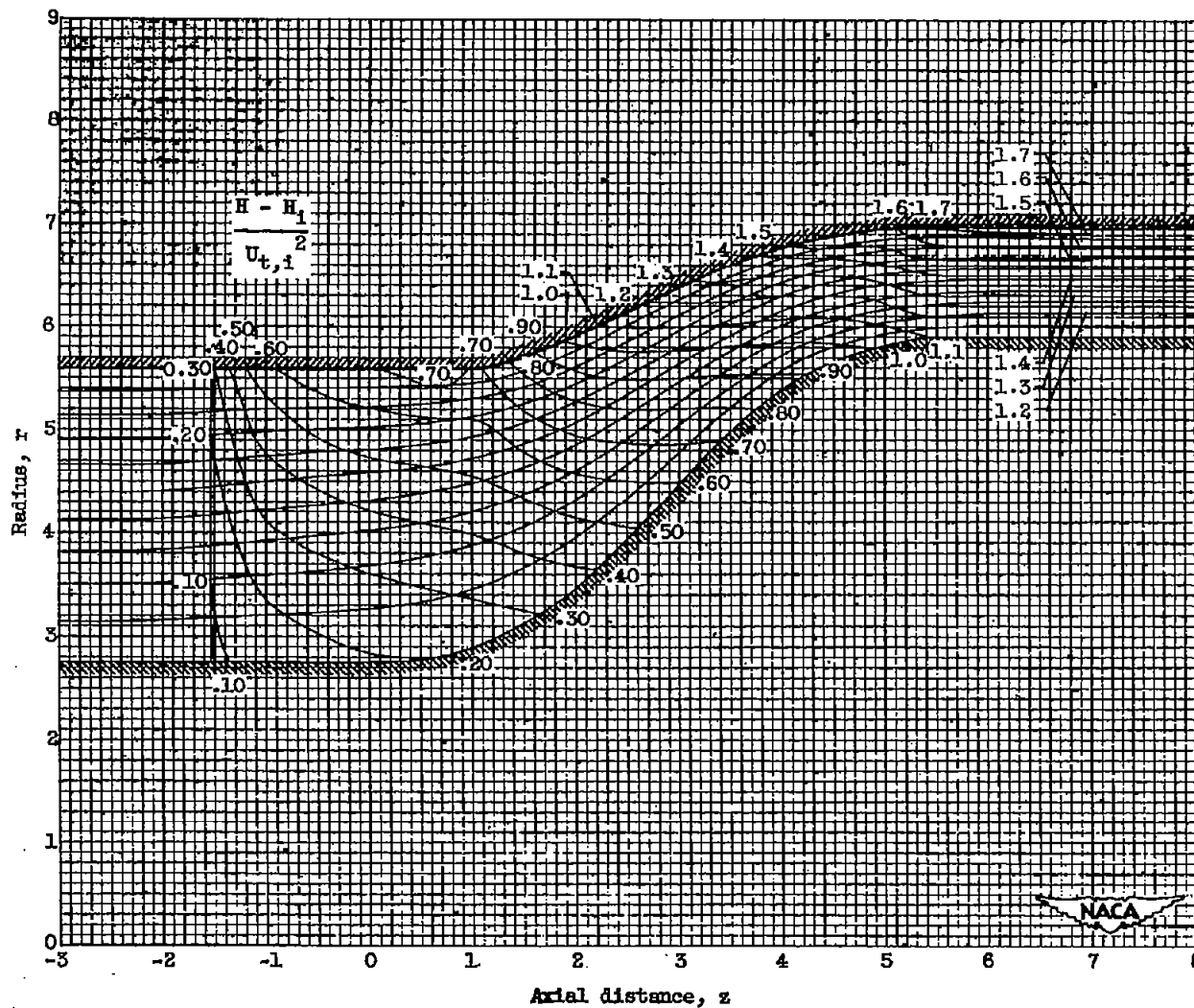


Figure 13.- Meridional projection of contours of constant total enthalpy superposed on streamlines for compressible solution. (An overlay of this fig. is enclosed.)

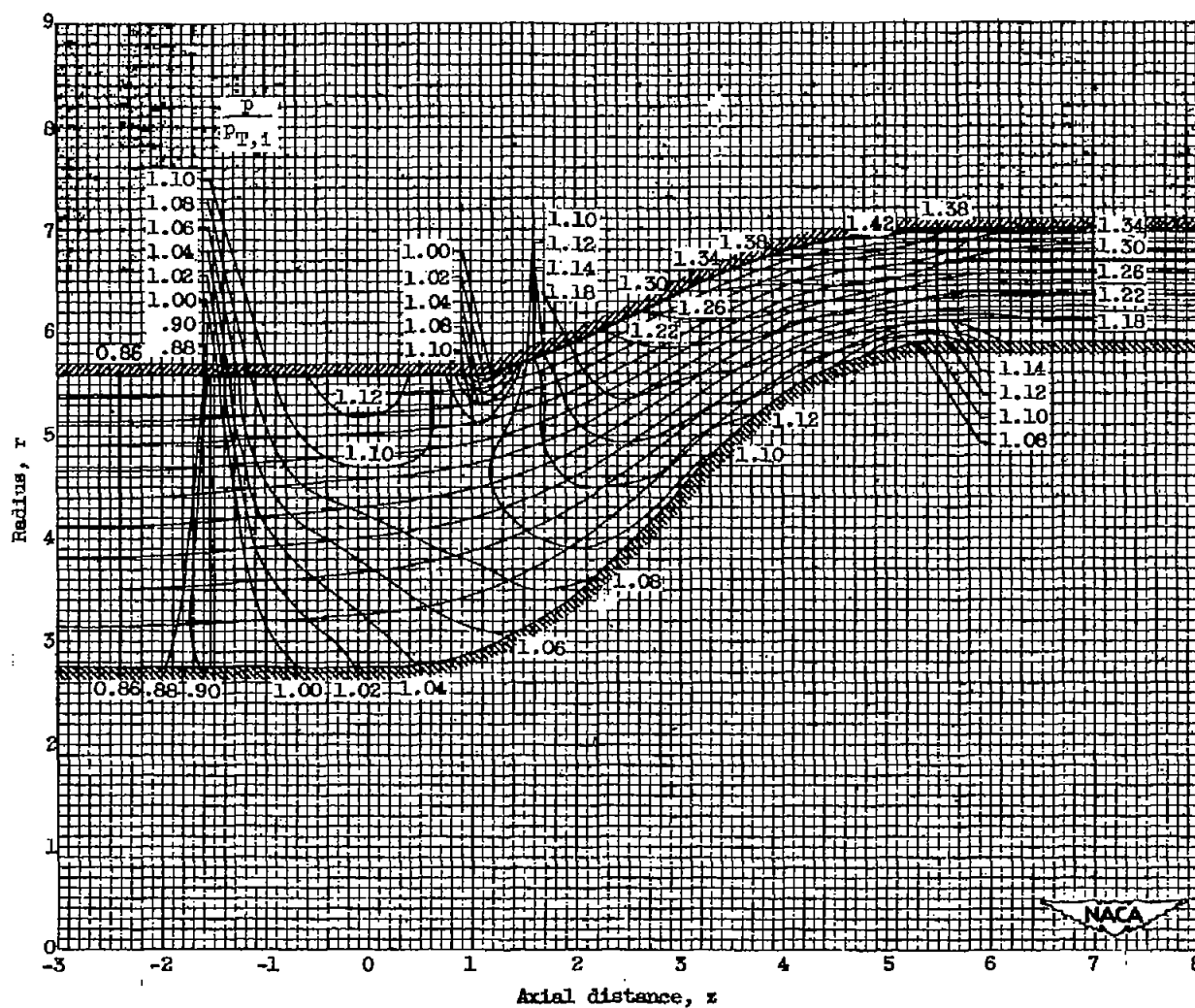


Figure 14.- Meridional projection of contours of constant pressure superposed on streamlines for compressible solution. (An overlay of this fig. is enclosed.)

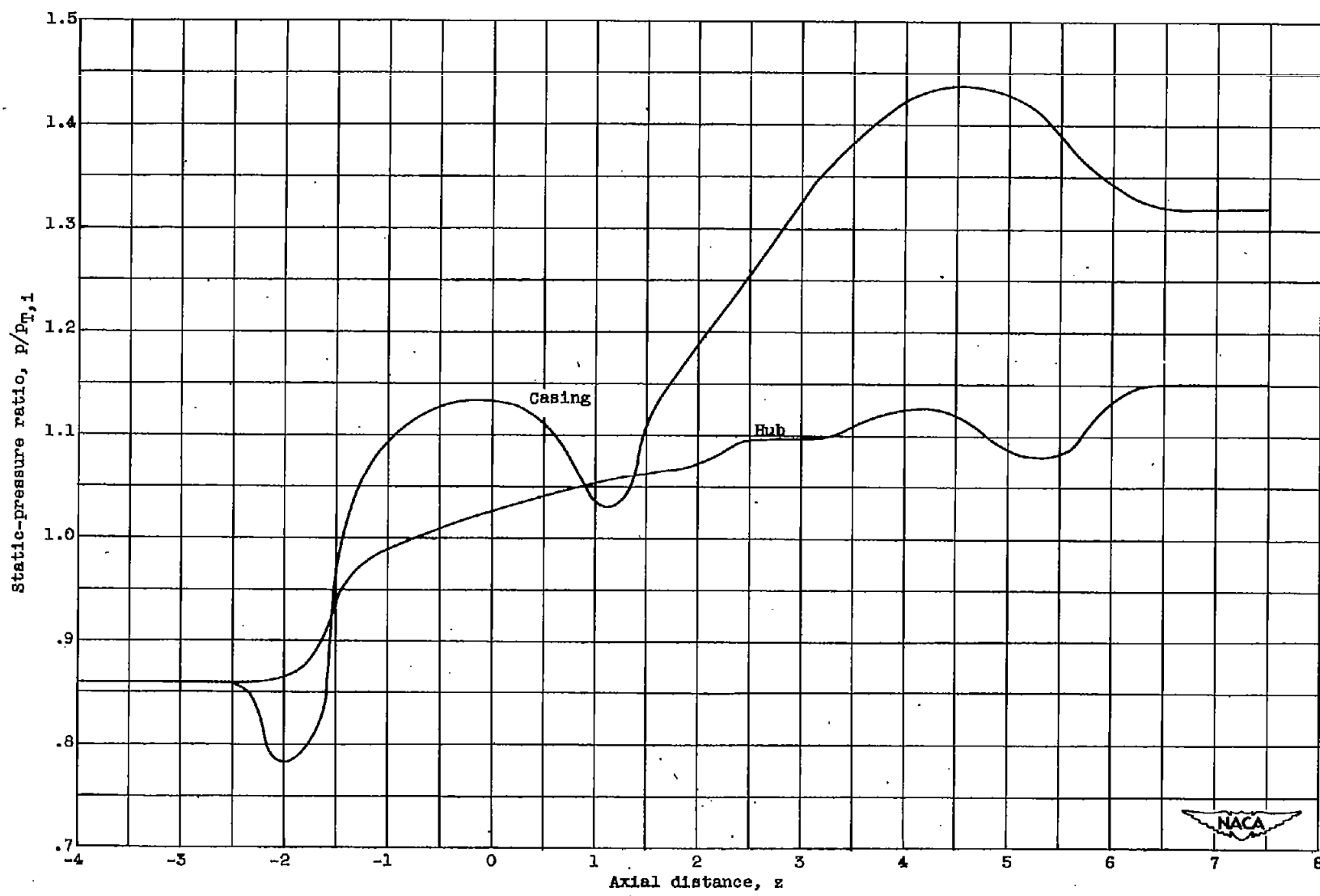


Figure 15. - Variation of static pressure along casing and hub walls for compressible solution.

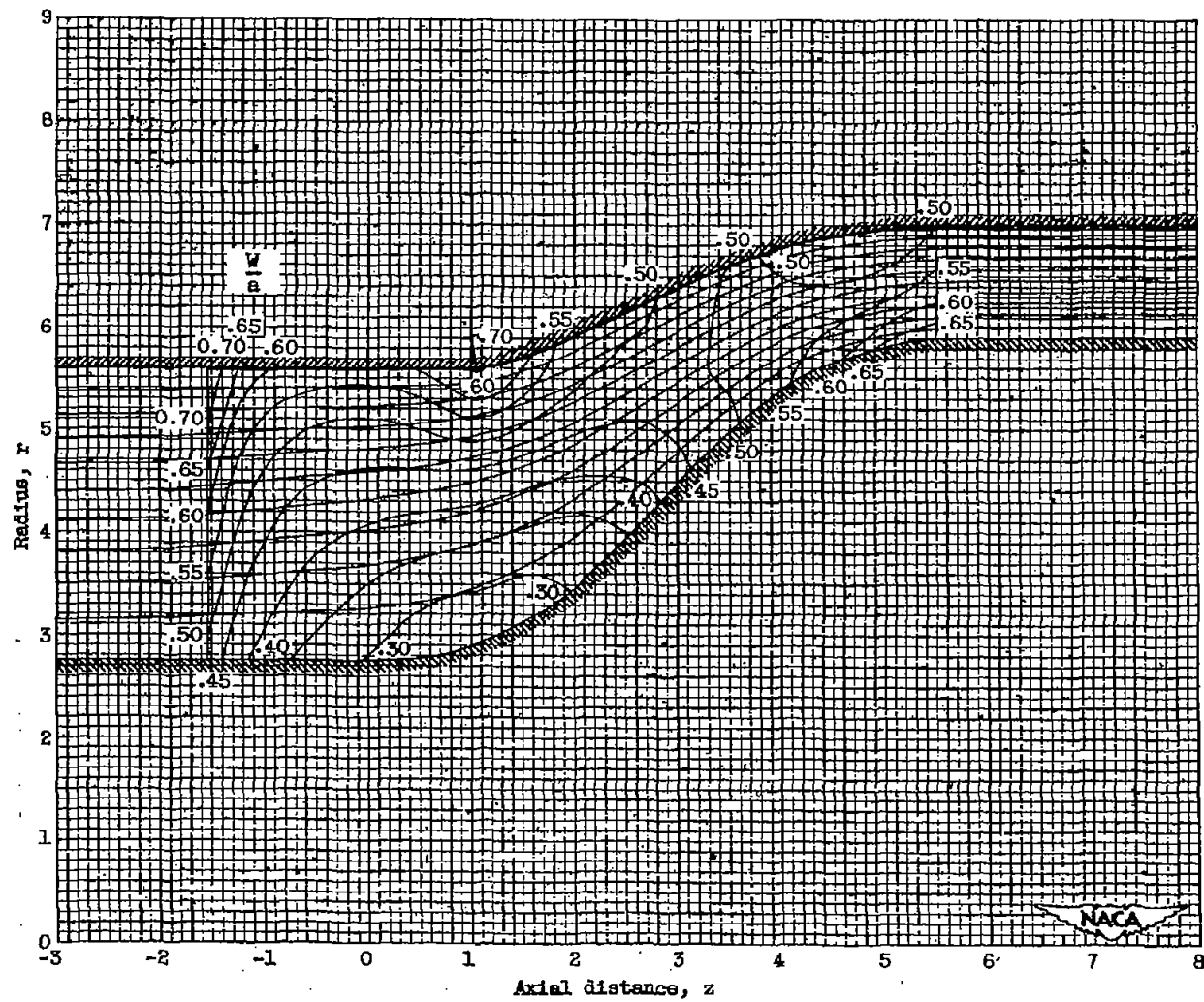


Figure 16. - Meridional projection of contours of constant relative Mach number superposed on streamlines for compressible solution.

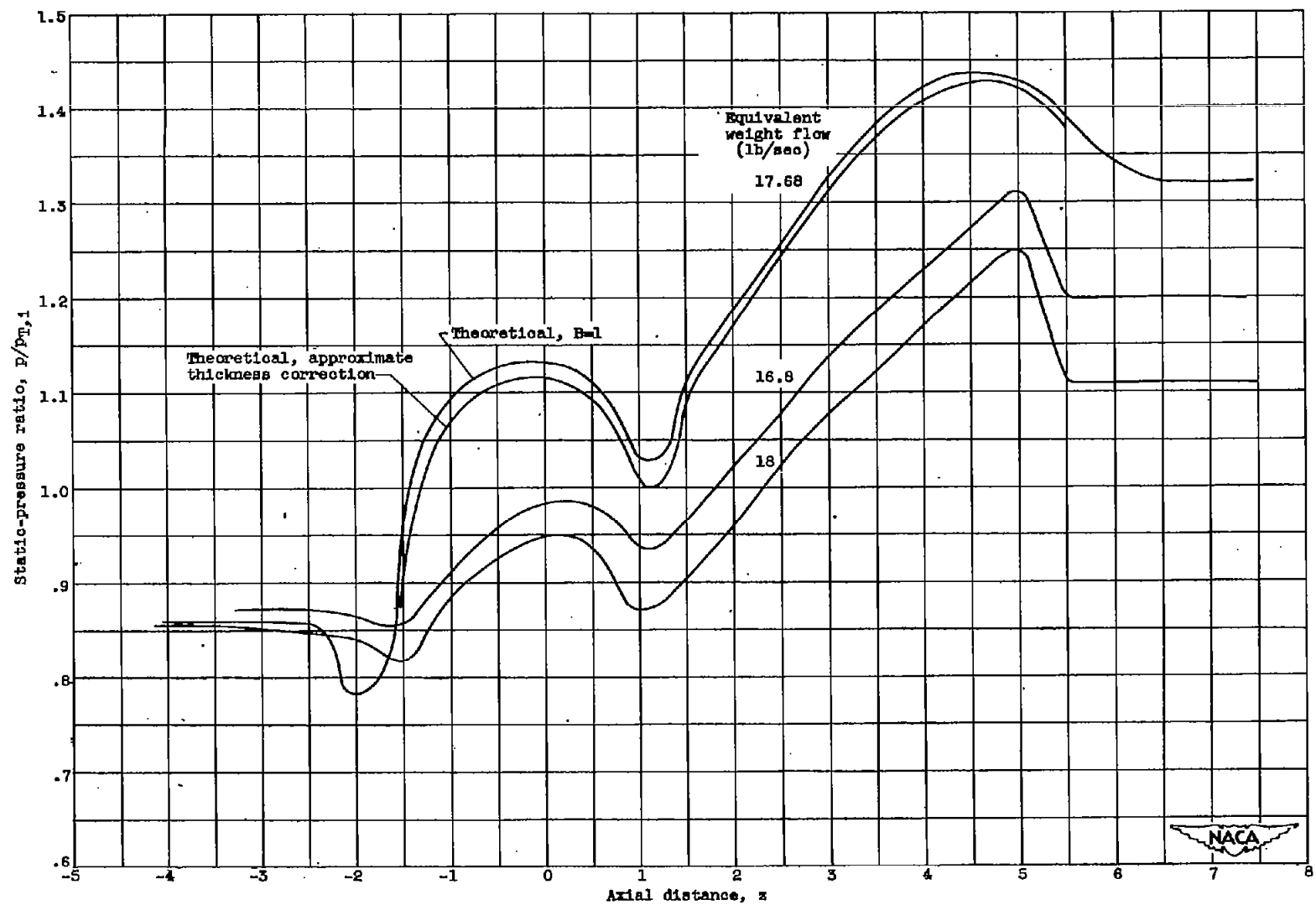


Figure 17. - Comparison of theoretical and experimental variation of static pressure along casing wall for compressible solution.  
 $M_1 = 0.45$ ;  $U_{t,c}/\theta = 987$  feet per second.

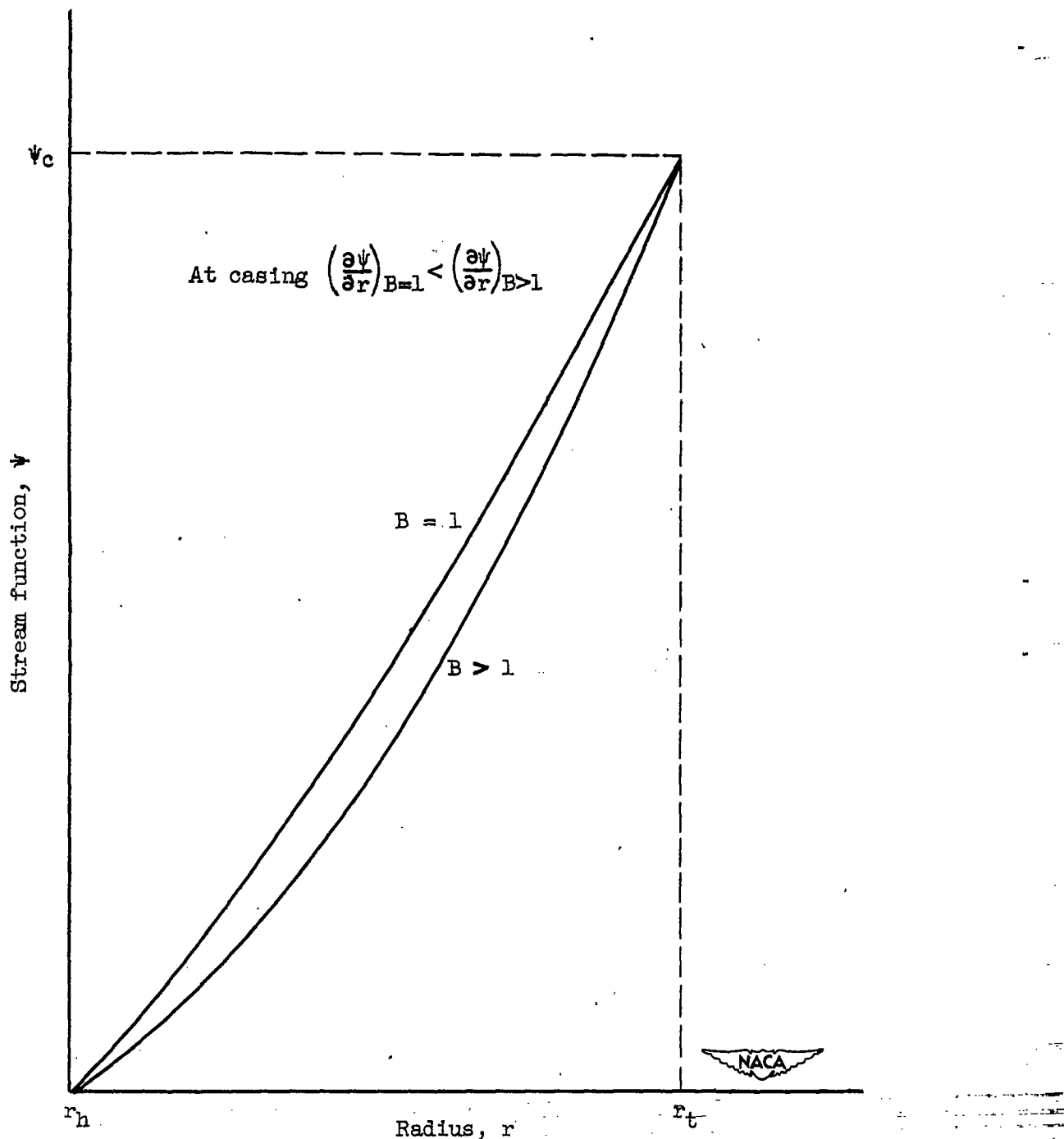


Figure 18. - Radial variation of stream function with constant and variable blade thickness factor.

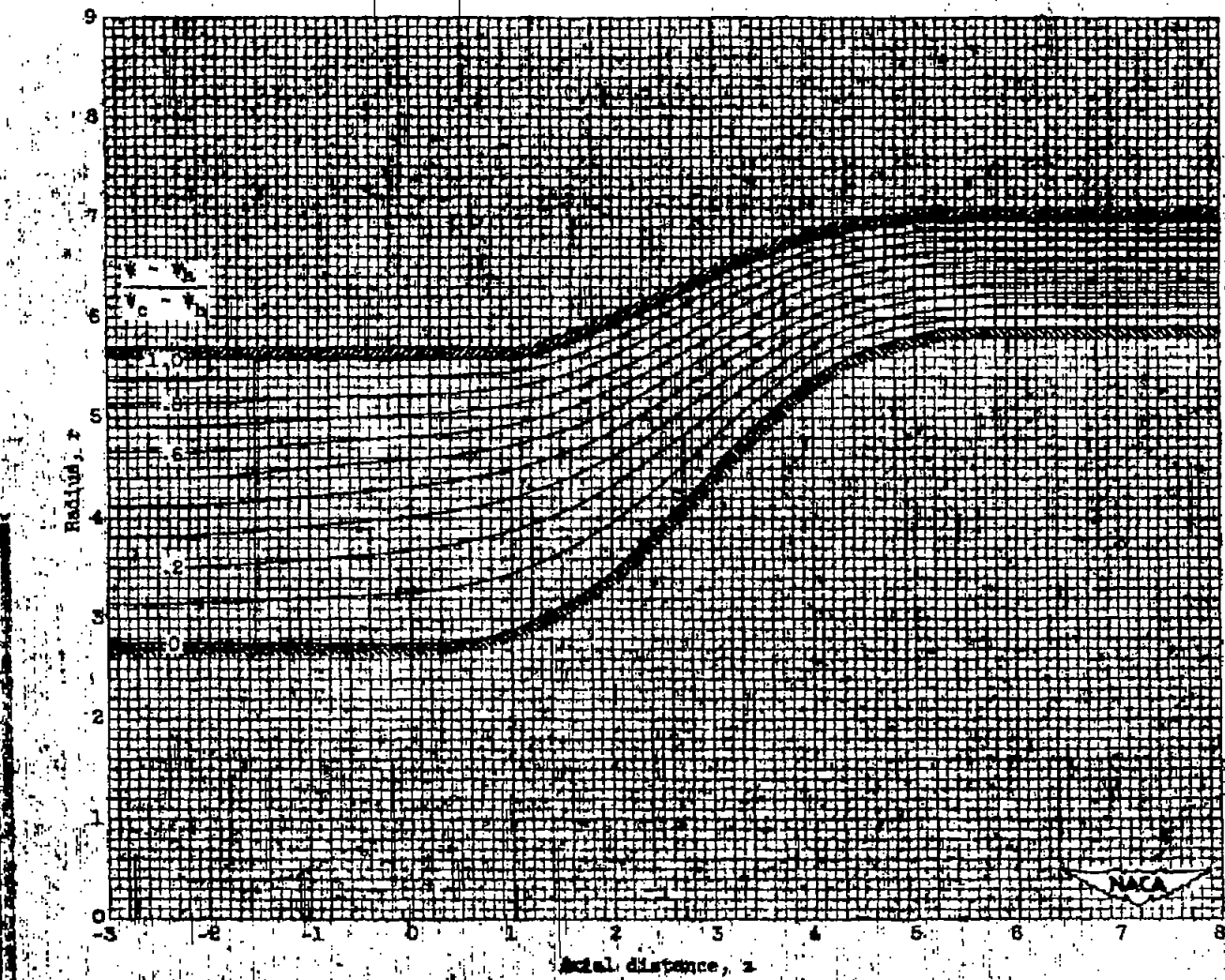
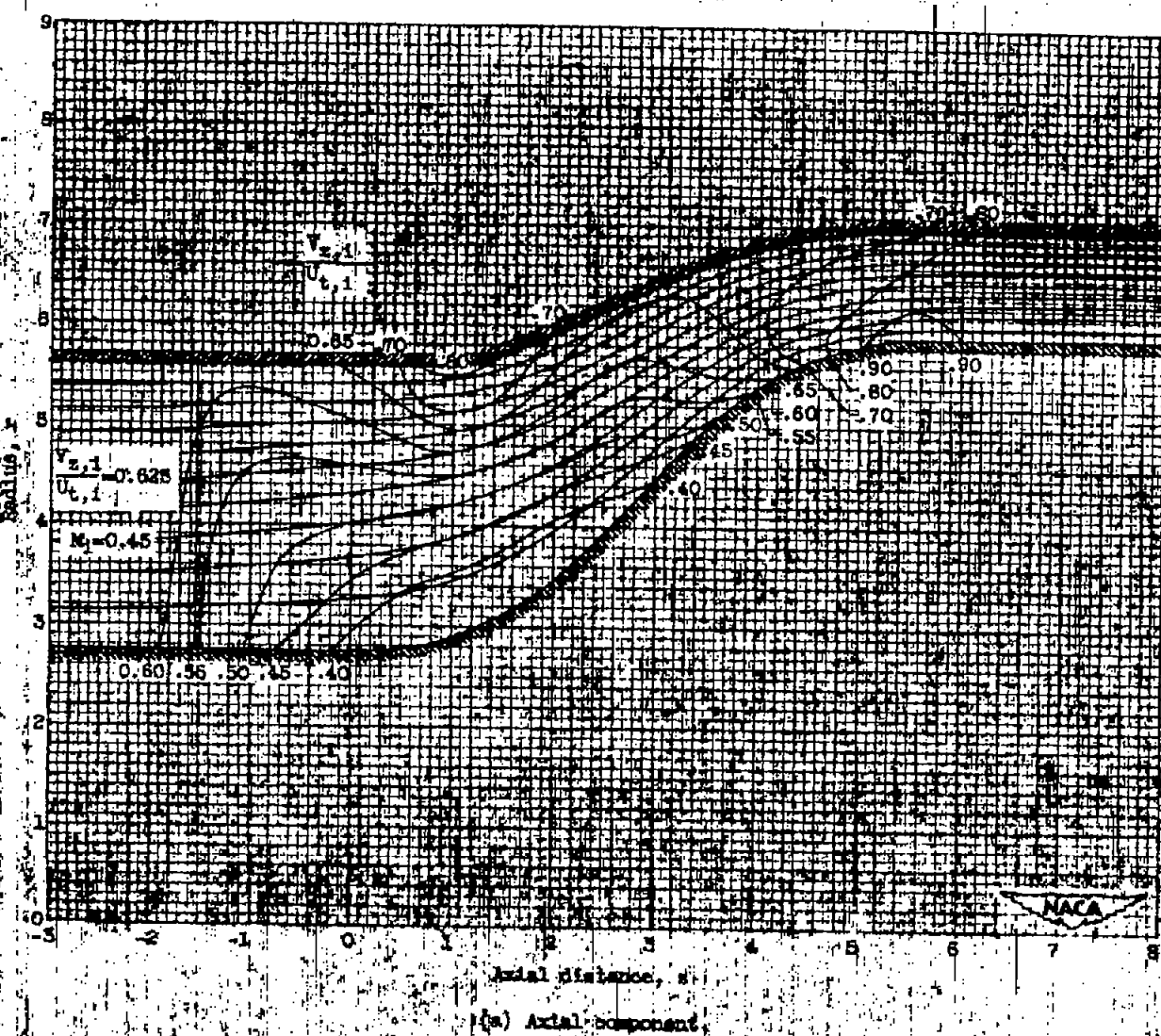
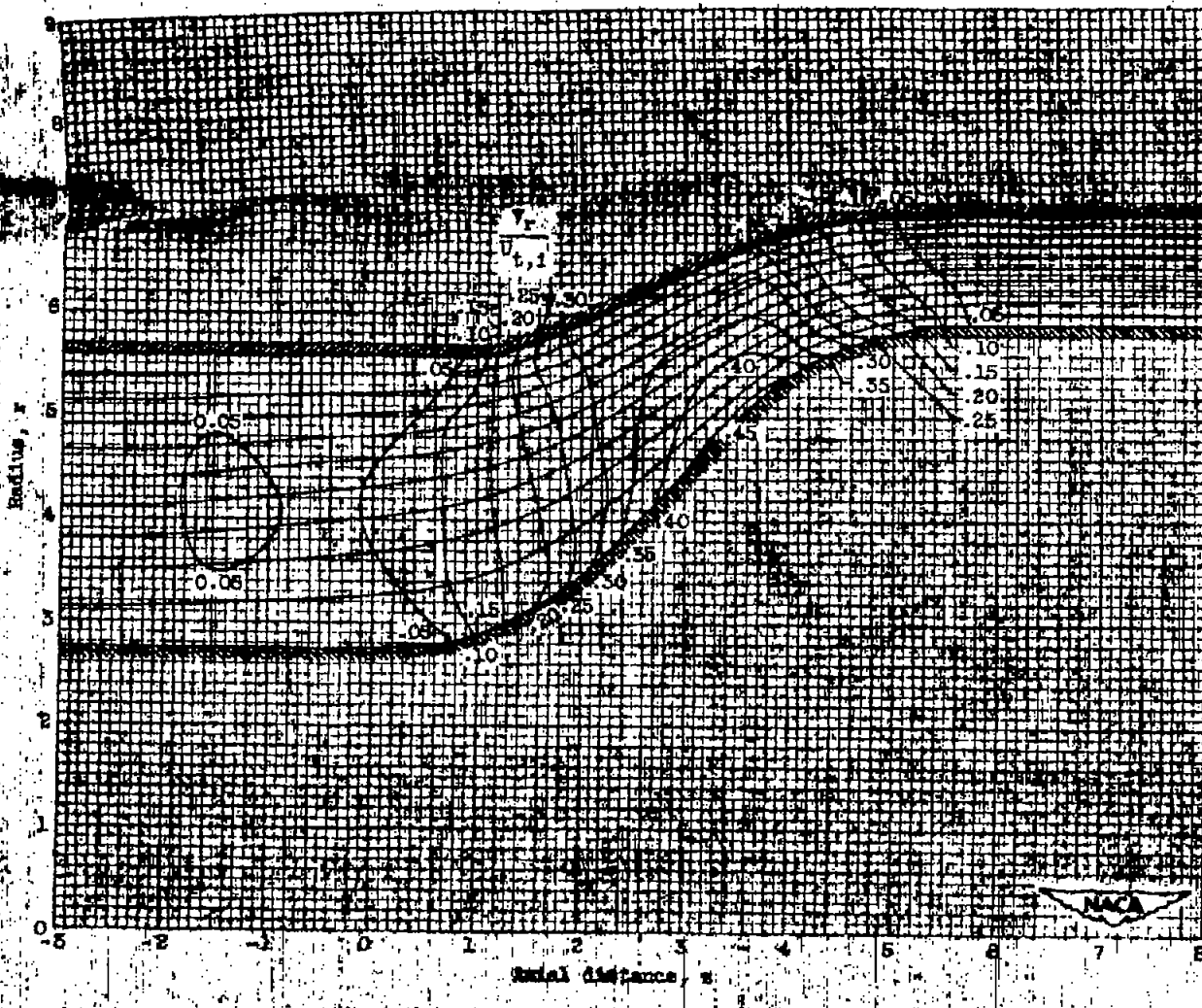


Figure 10. - Radial projection of streamlines obtained in compressible solution.



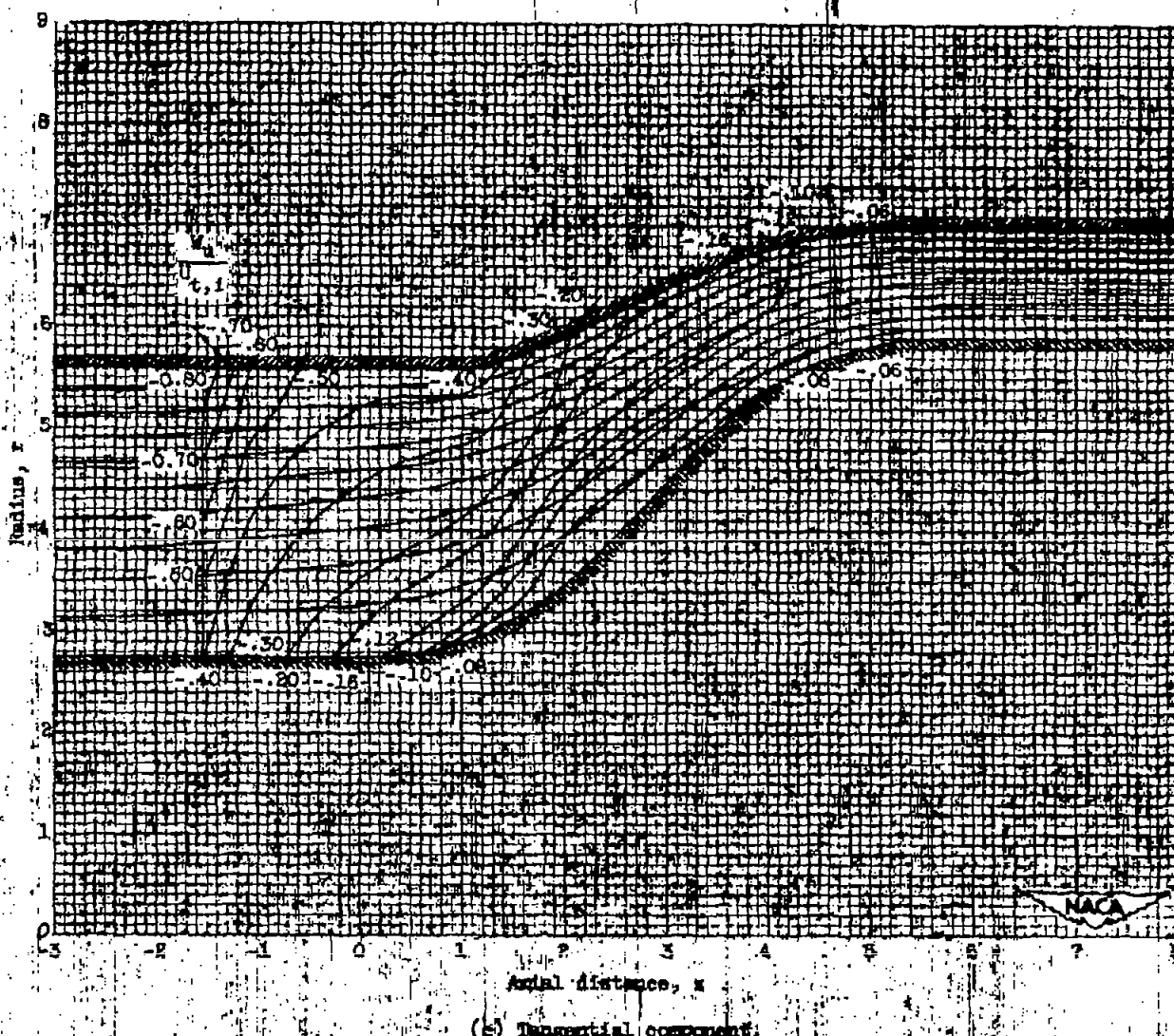
(a) Axial component,

Figure 11. Meridional projections of constant velocity contours superposed on streamlines for compressible solution.



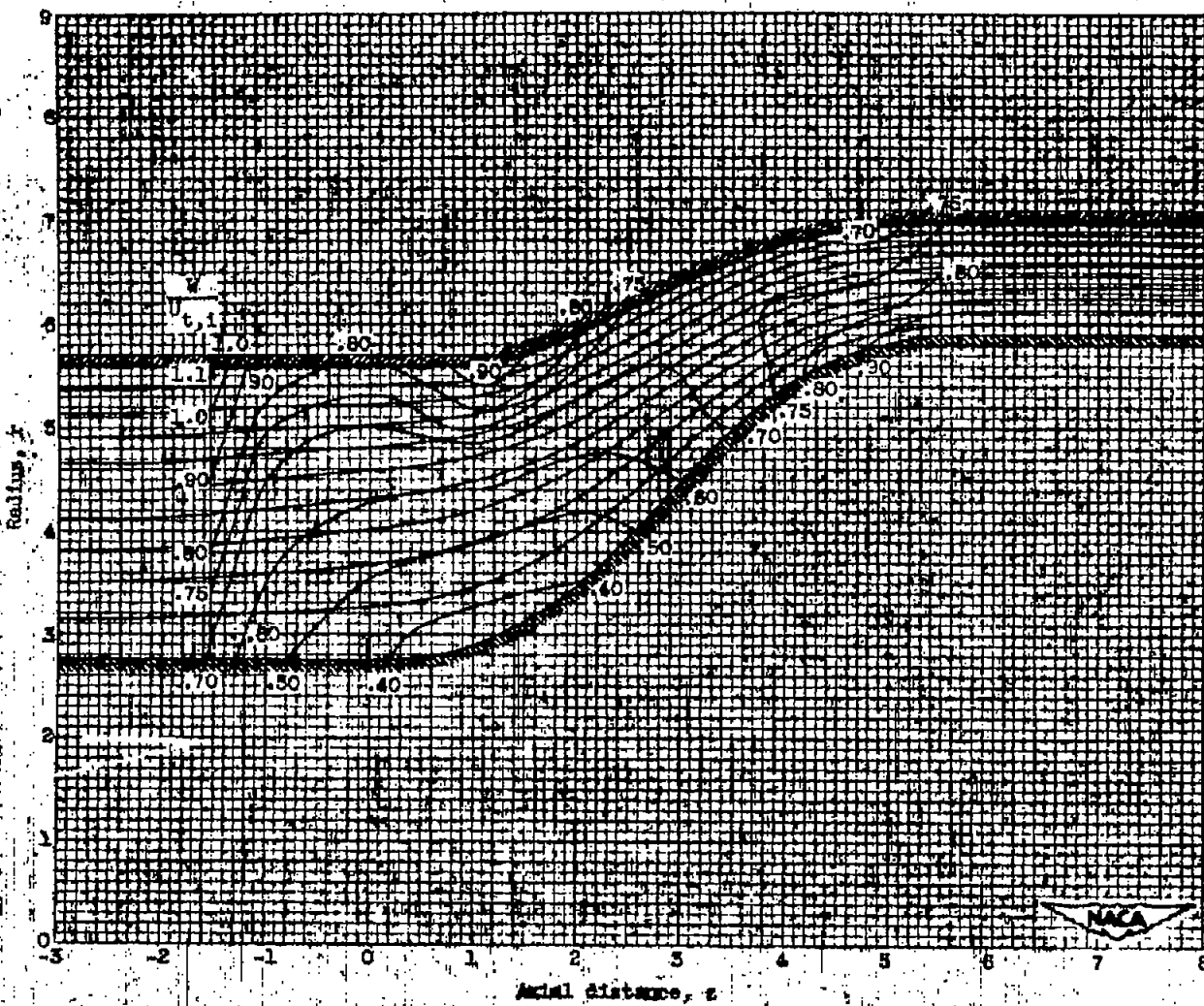
(b) Radial component.

Figure 11. - Continued. Meridional projections of constant velocity contours superposed on streamlines for compressible solution.



(e) Tangential component.

Figure 11. Contoured. Meridional projections of constant velocity contours superposed on streamlines for compressible solution.



(d) Resultant relative velocity.

Figure 11. Calculated meridional projections of constant velocity contours superposed on streamlines for compressible solutions.

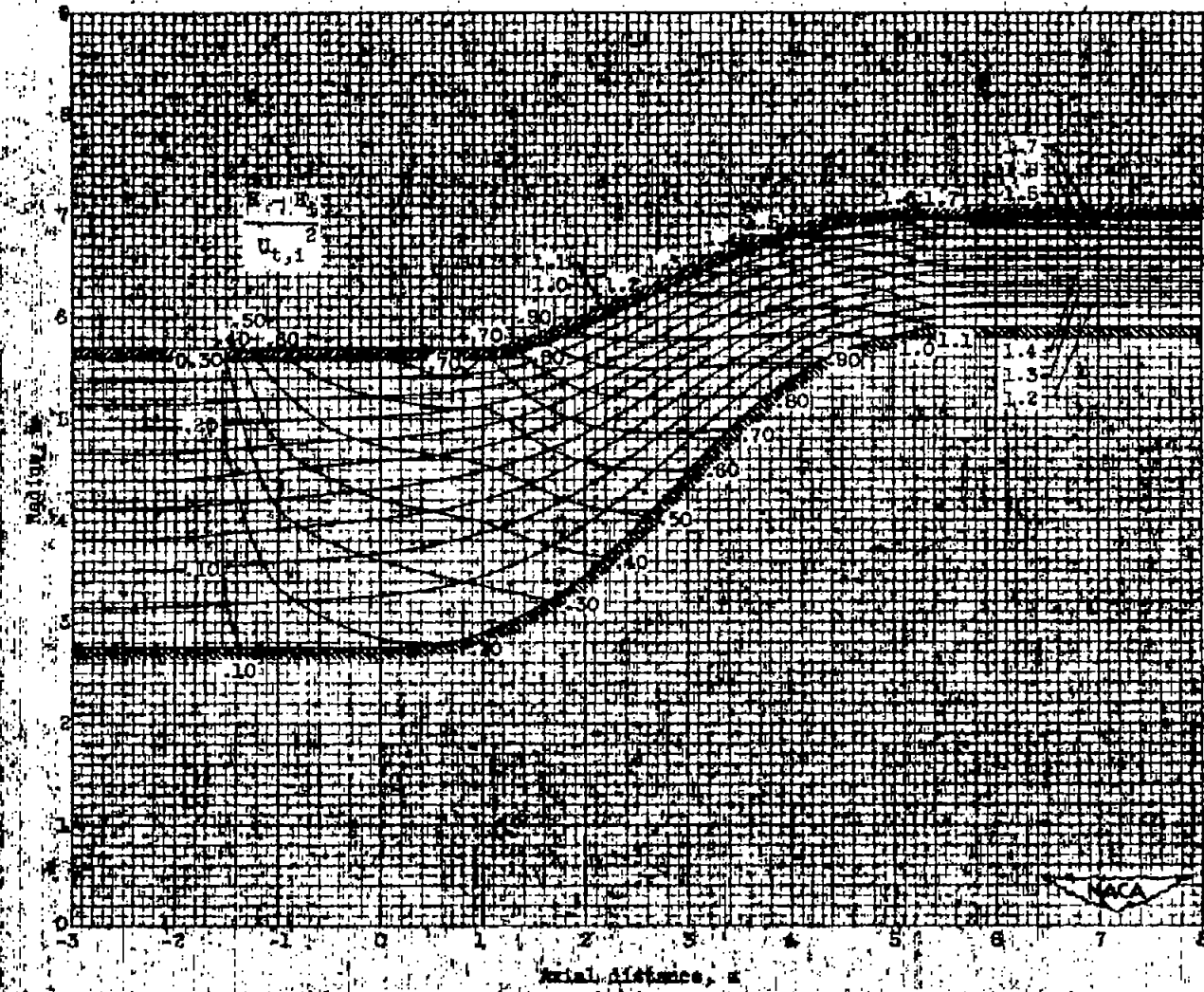


Figure 13. - Meridional projection of contours of constant total enthalpy superposed on streamlines for transonic solution.

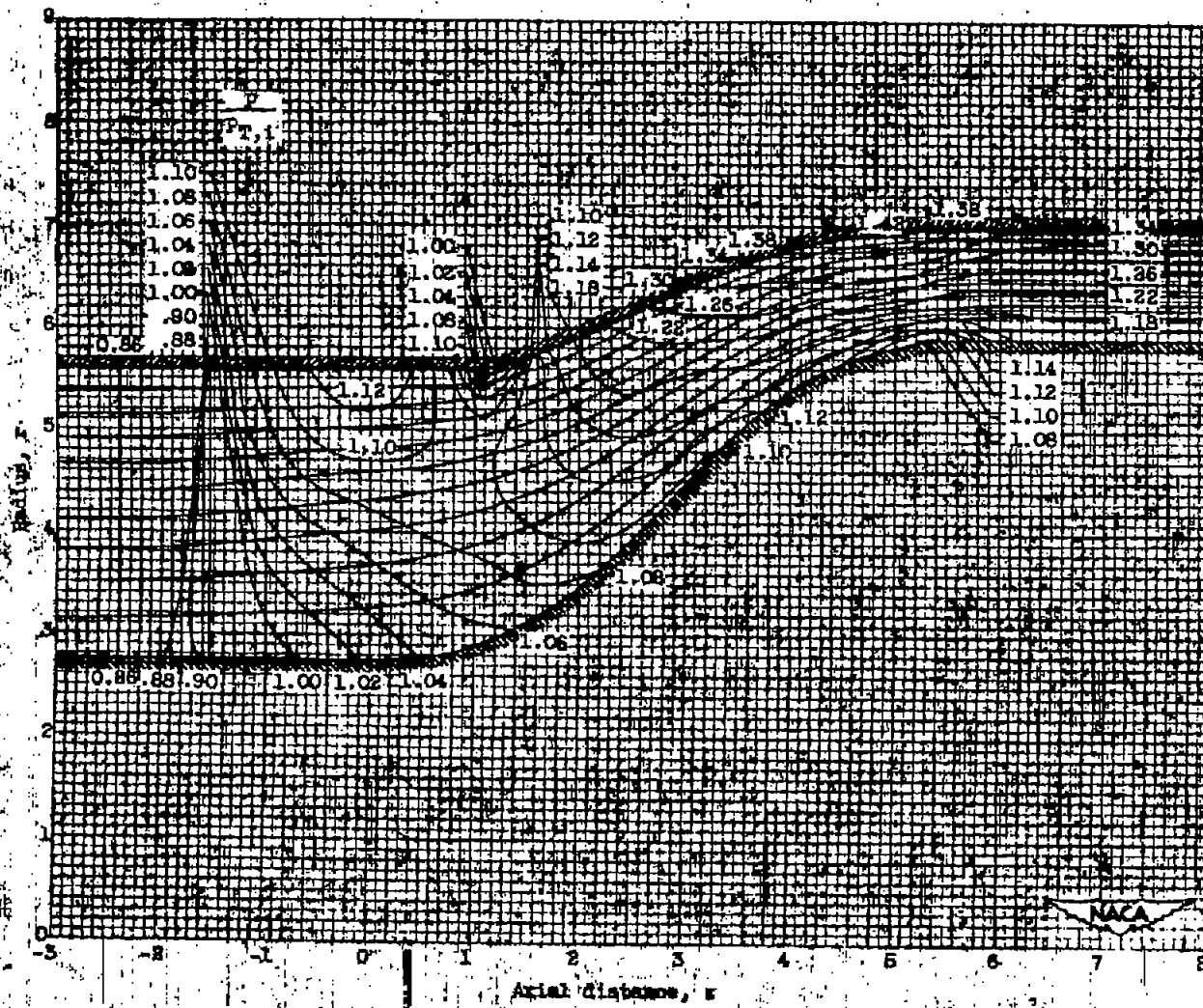


Figure 14. Meridional projection of contours of constant pressure superposed on streamlines for compressible solution.